The Astrophysical Journal, 1007:198 (22pp), 2026 August 20 https://doi.org/10.3847/1538-4357/ae89ad

Direct Retrieval of Protoplanetary Disk Dust Properties Using Auto-differentiable Gaussian Processes and Their Application to the HD 169142 Disk

Tomohiro C. Yoshida[1,2], Enrique Macías[3], Giovanni Rosotti[2], Stefano Facchini[2], Elena Viscardi[3], and Kiyoaki Doi[4]
[1] National Astronomical Observatory of Japan, 2-21-1 Osawa, Mitaka, Tokyo 181-8588, Japan; tomohiroyoshida.astro@gmail.com
[2] Dipartimento di Fisica, Università degli Studi di Milano, Via Celoria 16, 20133 Milano, Italy
[3] European Southern Observatory (ESO), Karl-Schwarzschild-Straße 2, Garching bei Múnchen, Germany
[4] Max-Planck Institute for Astronomy (MPIA), Kónigstuhl 17, 69117 Heidelberg, Germany
Received 2026 March 24; revised 2026 June 26; accepted 2026 July 11; published 2026 August 19

Abstract

Retrieving dust properties in protoplanetary disks, including the surface density distribution, temperature, and grain size distribution, is a fundamental task in observational studies of planet formation. While multiwavelength analysis of the spectral energy distribution (SED) using interferometers such as the Atacama Large Millimeter/submillimeter Array (ALMA) is a powerful diagnostic tool, traditional methods are often hindered by strong biases arising from a limited imaging beam size. In this paper, we present a new retrieval framework for dust disk properties designed to overcome this challenge. We assume that the underlying physical structures are expressed as sample paths from Gaussian processes, compute the radial intensity distributions at observed wavelengths, and produce one-dimensional visibility models. The models are compared with the observed data and the posterior distributions are sampled via the Markov Chain Monte Carlo method. The whole procedure is implemented in JAX, which enables end-to-end auto-differentiation and significantly accelerates the inference. We validate our methodology using mock datasets, and find that the results are not strongly biased and better reproduce the input profiles. We also demonstrate its capabilities through an application to ALMA Band 3, 6, and 9 observations of the HD 169142 disk, revealing a new complex structure. Our developed code is publicly available as a Python module, Flexible Radial Analysis of Protoplanetary Disks. This framework provides a next-generation infrastructure for disk SED modeling, enabling high-precision studies of the physical environments in which planets form. ?

Unified Astronomy Thesaurus concepts: Protoplanetary disks (1300); Planet formation (1241)

1. Introduction

Retrieving physical quantities in protoplanetary disks is vital for understanding the mechanisms of planet formation. Specifically, characterizing the radial distribution and grain growth of dust grains is a central objective in disk studies. Recent advancements in instrumentation, most notably the Atacama Large Millimeter/submillimeter Array (ALMA), have enabled the characterization of the dust disk properties at high angular resolution with multiple frequencies (e.g., C. Carrasco-González et al. 2019; E. Macías et al. 2019, 2021; A. Sierra et al. 2021, 2024, 2025; G. Guidi et al. 2022; T. Ueda et al. 2022; S. Ohashi et al. 2023; S. Zhang et al. 2023; A. S. Carvalho et al. 2024; O. M. Guerra-Alvarado et al. 2024; F. Zagaria et al. 2025).

In typical studies, the spectral energy distribution (SED) is measured as a function of radius from the central star. These data are then fitted with specific SED models to derive key parameters such as the dust surface density, temperature, and grain size distribution. While this approach is straightforward, it is subject to several critical limitations.

First, many analyses assume that the observed intensity directly represents the intrinsic intensity. While this approximation may hold for well-resolved sources, it becomes problematic in marginally resolved cases where beam convolution effects are significant (e.g., D. Li et al. 2024). Second, conventional methods often require images or radial profiles to be processed at the same spatial resolution. This requirement is sometimes technically challenging; for instance, long-wavelength observations typically achieve significantly lower spatial resolution than higher wavelengths, despite their importance. Consequently, datasets are often smoothed to match the coarsest resolution, which can lead to misinterpretation of radial substructures. It is notable that a multistage fitting strategy to mitigate some of these resolution-related issues has been recently proposed (E. M. Viscardi et al. 2025; F. Zagaria et al. 2025). Third, a standard imaging algorithm, CLEAN, can introduce systematic uncertainties due to the sidelobes, potentially leading to underestimated errors or biases in the retrieved physical quantities. A more robust approach would be to fit the model directly to the interferometric visibilities, a fundamental observable of the interferometer. Finally, previous methods typically treat observational noise as being spatially or radially independent. In reality, flux scaling uncertainties, which often dominate the error budget, are radially correlated and must be properly accounted for.

In this paper, we propose a new retrieval framework for dust disk properties that addresses these limitations. Our approach employs Gaussian processes (GPs) to construct the underlying physical structures and utilizes auto-differentiation for accelerated posterior sampling from the visibility data. We have developed an open-source Python module, Flexible Radial Analysis of Protoplanetary Disks (FRAP), to implement the methodology presented herein.

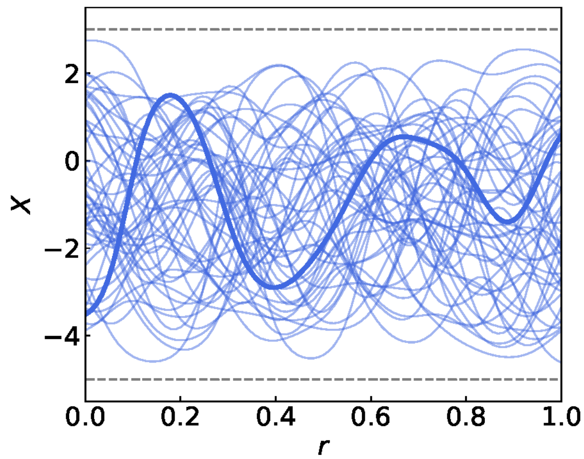

Figure 1. Illustrative radial profiles of an arbitrary quantity X sampled from the GP prior after applying the sigmoid transformation. We assume an RBF kernel with a length scale of $l_X = 0.1$. A single representative sample is shown as a solid curve, while the ensemble of 20 samples demonstrates the prior's flexibility. The horizontal dashed lines indicate the boundaries $X_{\max}$ and $X_{\min}$.

The paper is organized as follows. In Section 2, we describe our modeling framework. In Section 3, we validate FRAP using mock datasets. We then apply this method to real ALMA observations of the HD 169142 disk in Section 4. In Section 5, we discuss the performance of the method and the scientific implications for the HD 169142 disk. Finally, we summarize our findings in Section 6.

2. Method

The primary objective of FRAP is to retrieve the radial distribution of dust properties, such as the dust surface density, grain size distribution, and temperature, from interferometric visibilities directly. Throughout this section, we assume that the disk is axisymmetric and that the observed visibilities have been deprojected and have real part values as a function of the deprojected *uv* distance or radial visibility profiles. We describe the practical process for this manipulation in Section 3.3.1.

The architecture of FRAP consists of three main stages. First, the radial profiles of the physical quantities are represented as samples from a nonparametric GP. Second, the SED at each radius is computed using a reduced radiative transfer model, which generates radial intensity profiles at each wavelength. Finally, these intensity profiles are Hankel transformed to obtain the corresponding radial visibility profiles.

The entire modeling framework is implemented in JAX (J. Bradbury et al. 2018), a Python library optimized for high-performance machine learning and numerical computing. This choice enables end-to-end automatic differentiation of the model; for example, the gradient of a specific visibility value with respect to the dust surface density at a given radius can be computed efficiently. This auto-differentiation capability significantly accelerates the sampling of the posterior distribution via gradient-based Markov Chain Monte Carlo (MCMC) methods. Specifically, it enables the retrieval of dust properties with the high degree of flexibility afforded by GPs, which would otherwise be computationally prohibitive. In our practical implementation, we utilize numpyro (E. Bingham et al. 2019; D. Phan et al. 2019) to perform the posterior sampling.

2.1. Radial Profile Modeling with Gaussian Processes

We employ a GP as a prior for the radial profile of a given parameter $X(r)$, where r denotes the radius from the disk center. A GP is a multivariate normal distribution characterized by a covariance (kernel) matrix. In this study, we adopt the radial basis function (RBF) kernel for the parameter X:

$$K_X(r_1, r_2) = \exp\left(-\frac{(r_1 - r_2)^2}{2l_X^2}\right), \tag{1}$$

where r_1 and r_2 represent radial positions and l_X is the characteristic length scale.

To treat parameters with upper and lower boundaries, we reparameterize them. Specifically, we apply a sigmoid-like transformation such that $X(r)$ is mapped from its physical range $[X_{\min}, X_{\max}]$ to a latent space:

$$x(r) = \log\left\{1 - \frac{X(r) - X_{\min}}{X_{\max} - X_{\min}}\right\}, \tag{2}$$

where $X_{\min}$ and $X_{\max}$ are the prescribed minimum and maximum bounds for the parameter, respectively.

Figure 1 displays 20 sample radial profiles generated from this GP prior with $l_X = 0.1$ and the range defined by $(X_{\min}, X_{\max}) = (-5, 3)$ in arbitrary units to demonstrate the flexibility of GPs. These flexible curves serve as the prior distributions for the fitting process in FRAP.

2.2. Reduced Radiative Transfer Model

The GP framework described in Section 2.1 provides the nonparametric priors for the physical quantities we aim to retrieve. For the sake of clarity, we consider a model characterized by three free radial parameters in this and next sections: the dust surface density $\Sigma(r)$, the dust temperature $T(r)$, and the maximum dust grain size $a_{\max}(r)$. The dust grain size distribution $n(a)$ is assumed to follow a power law with an exponent q:

$$\frac{dn}{da} \propto \begin{cases} a^{-q} & (a_{\min} < a < a_{\max}), \\ 0 & (\text{otherwise}), \end{cases} \tag{3}$$

where we fix the minimum grain size to $a_{\min} = 0.1\ \mu$m.

Once the dust size distribution is defined, the absorption and effective scattering opacity profiles at each frequency ν, $\kappa_{\rm abs}(\nu, r)$ and $\kappa_{\rm sca,eff}(\nu, r)$, are calculated. While we adopt the DSHARP opacity model (T. Birnstiel et al. 2018) in this and next sections, FRAP can accommodate any user-defined opacity model that maps physical quantities (e.g., $a_{\max}$) to optical properties. From these opacities, we derive the radial profiles of the scattering albedo

$$\omega(\nu, r) = \frac{\kappa_{\rm sca,eff}}{\kappa_{\rm sca,eff} + \kappa_{\rm abs}}, \tag{4}$$

and the absorption optical depth

$$\tau(\nu, r) = \kappa_{\rm abs}\Sigma, \tag{5}$$

where the ν and r dependence is omitted on the right-hand sides for simplicity.

We approximate the radiative transfer using an isothermal, geometrically thin slab model. We employ the analytical solution derived by A. Sierra & S. Lizano (2020) using the two-stream approximation (e.g., K. Miyake & Y. Nakagawa 1993; H. B. Liu 2019; Z. Zhu et al. 2019) to calculate the emergent intensity at each radius:

$$I(\nu, r) = B(\nu, T)\left[1 - \exp\left(-\frac{\tau}{1-\omega}\right) + \omega\mathcal{F}(\tau, \omega)\right], \quad (6)$$

where $B(\nu, T)$ is the Planck function and $\mathcal{F}(\tau, \omega)$ is defined as

$$\mathcal{F}(\tau, \omega) = \frac{1}{\left(\sqrt{1-\omega} - 1\right)\exp\left(-\sqrt{\frac{3}{1-\omega}}\tau\right) - \left(\sqrt{1-\omega} + 1\right)} \times \left\{\frac{1 - \exp\left[-\left(\sqrt{3(1-\omega)} + 1\right)\frac{\tau}{1-\omega}\right]}{\sqrt{3(1-\omega)} + 1} + \frac{\exp\left[-\frac{\tau}{1-\omega}\right] - \exp\left[-\sqrt{\frac{3}{1-\omega}}\tau\right]}{\sqrt{3(1-\omega)} - 1}\right\}. \quad (7)$$

These expressions can be modified or replaced based on the user's specific requirements.

2.3. Hankel Transform and Visibilities

The radial intensity profiles at each wavelength, $I(\nu, r)$, are converted into one-dimensional visibility profiles using a discrete Hankel transform. The detailed derivation of this numerical approach is based on N. Baddour & U. Chouinard (2015) and J. Jennings et al. (2020); here, we briefly summarize the implementation. We utilize a Fourier–Bessel series expansion to express the model visibilities:

$$\mathcal{V}_{\rm mod}(\nu, q_{{\rm c},k}) = \frac{4\pi R_{\rm out}^2}{j_{0,N+1}^2}\sum_{i=1}^{N} J_0\left(\frac{j_{0,k}j_{0,i}}{j_{0,N+1}}\right) \times \frac{A_{\rm eff}(\nu, r_{{\rm c},i})I(\nu, r_{{\rm c},i})}{J_1^2(j_{0,i})}, \quad (8)$$

where $R_{\rm out}$ is the outer radius of the disk, $J_0(x)$ and $J_1(x)$ are the zeroth- and first-order Bessel functions of the first kind, respectively, and $j_{0,i}$ is the ith root of $J_0(x)$ (i.e., $J_0(j_{0,i}) = 0$). We define $R_{\rm out}$ such that the intensity beyond $r > R_{\rm out}$ is zero. The terms $q_{{\rm c},k}$ and $r_{{\rm c},i}$ represent the collocation points in the spatial frequency and spatial domains:

$$q_{{\rm c},k} = \frac{j_{0,k}}{2\pi R_{\rm out}}, \quad (9)$$

$$r_{{\rm c},i} = \frac{j_{0,i}}{j_{0,N+1}}R_{\rm out}. \quad (10)$$

where $A_{\rm eff}(\nu, r_{c,i})$ is the effective primary beam factor at each disk radius. This has not been considered in the previous studies, but is introduced and discussed in Appendix A. In practice, we adopt the primary beam implemented in the Common Astronomy Software Application (CASA) version 6.7 (CASA Team et al. 2022).[5]

While the intensities are evaluated at the collocation points $r_{{\rm c},i}$, it is necessary to compute the visibilities at the specific uv distances that match the observations. To achieve this, we employ

$$\mathcal{V}_{\rm mod}(\nu, q_l) = \sum_{i=1}^{N} H_i(q_l)I(\nu, r_{{\rm c},i}), \quad (11)$$

where

$$H_i(q_l) = \frac{4\pi R_{\rm out}^2 A_{\rm eff}(\nu, r_{{\rm c},i})}{j_{0,N+1}^2 J_1^2(j_{0,i})} J_0\left(2\pi q_l R_{\rm out}\frac{j_{0,i}}{j_{0,N+1}}\right). \quad (12)$$

Here, q_l corresponds to the uv distance of the lth data point at frequency ν. This formulation assumes that the disk intensity vanishes for all radii $r \geqslant R_{\rm out}$.

2.4. Visibility Comparison and Posterior Sampling

The modeled visibilities ($\mathcal{V}_{\rm mod}(\nu, q_l)$, Equation (11)) are compared directly with the observed visibilities, $\mathcal{V}_{\rm obs}(\nu, q_l)$. Note that the visibilities are purely real since we assume an axisymmetric disk. We define the log-likelihood function as

$$\log P = -\frac{1}{2}\sum_{m,l}\left(\frac{\mathcal{V}_{\rm obs}(\nu_m, q_l) - f_m\mathcal{V}_{\rm mod}(\nu_m, q_l)}{\sigma_{\mathcal{V}}(\nu_m, q_l)}\right)^2. \quad (13)$$

The summation is performed over all uv points across all observed frequencies ν_m. The factor f_m represents the flux scaling uncertainty, which we treat as a free parameter sampled from a lognormal prior. This factor is assumed to be constant within a single observational epoch where a common absolute flux calibration applies. If multiple independent datasets are combined, a different f_m is assigned to each set to account for independent calibration uncertainties. $\sigma_{\mathcal{V}}(\nu_m, q_l)$ is the uncertainty associated with the visibility point.

To retrieve the physical parameters, we utilize the `numpyro` probabilistic programming library (E. Bingham et al. 2019; D. Phan et al. 2019). We use the No-U-Turn Sampler (NUTS; M. D. Hoffman & A. Gelman 2014), a variant of the Hamiltonian Monte Carlo algorithm. The specific hyperparameters for the MCMC procedure, such as the number of warm-up and sampling steps, are adjusted depending on the complexity of the problem.

3. Injection–Recovery Test Using Mock Data

3.1. Mock Data

In this section, we perform an injection–recovery test using mock datasets to evaluate the performance of our retrieval framework. We first construct a mock disk model. This model mimics the characteristic features of the HD 169142 disk, which we analyze in Section 4, although it is not intended to be a high-fidelity physical representation. First, the dust surface density is defined as a sum of four Gaussian rings:

$$\Sigma_{\rm d}(r) = \sum_{i=1}^{4}\Sigma_{0,i}\exp\left(-\frac{(r-r_i)^2}{2w_i^2}\right), \quad (14)$$

where the peak surface densities are $\Sigma_{0,i} = (10, 1, 1.5, 0.1)$ g cm^{-2}, the ring center radii are $r_i = (26.2, 57.8, 64.7, 76.6)$ au, and the widths are $w_i = (2, 1, 1, 2)$ au. The radial positions r_i correspond to the ring locations in HD 169142 identified by E. Macías et al. (2019) and S. Pérez et al. (2019). The temperature profile is

[5] See also https://help.almascience.org/kb/articles/how-do-i-model-the-alma-primary-beam-and-how-can-i-use-that-model-to-obtain-the-sensitivity-pr.

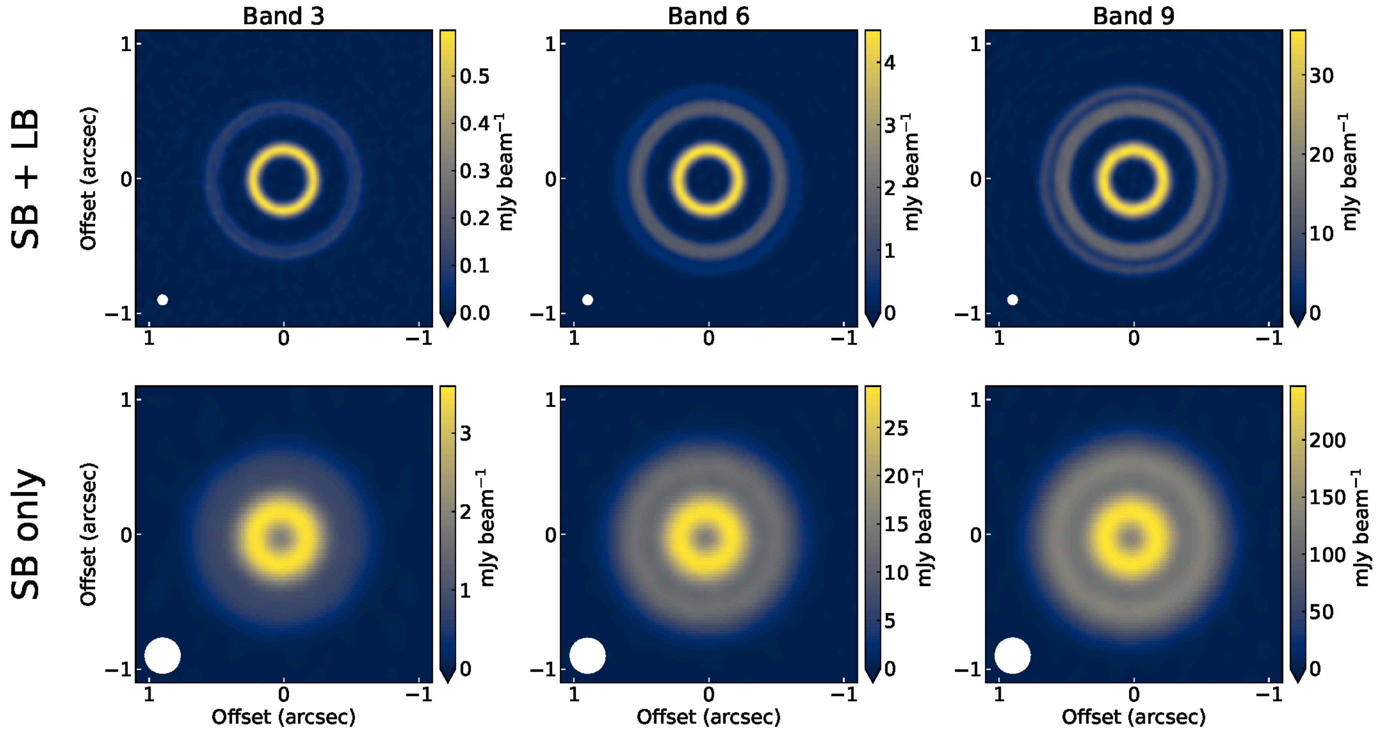

Figure 2. CLEAN images of the mock datasets across three ALMA bands. The upper and lower panels show the SB + LB and SB-only datasets, respectively. The white ellipses in the bottom-left corners indicate the synthesized beam sizes. Note that all images within each row are smoothed to a common beam (∼0″06 for SB + LB and ∼0″25 for SB-only data). Note that the images are not deprojected.

prescribed as

$$T(r) = 77\left(\frac{r}{10\ \mathrm{au}}\right)^{-0.5}\ \mathrm{K}, \tag{15}$$

following E. Macías et al. (2019). For the maximum grain size, we assume a step function:

$$a_{\max}(r) = \begin{cases} 3.0\ \mathrm{cm} & (r < 46\ \mathrm{au}), \\ 0.1\ \mathrm{cm} & (r \geqslant 46\ \mathrm{au}). \end{cases} \tag{16}$$

We adopt a power-law index of $q = 3.5$ for the grain size distribution and use the default DSHARP dust opacity model (T. Birnstiel et al. 2018).

Using this physical structure and the radiative transfer model described in Section 2.2, we generated the radial intensity profiles at ALMA Bands 3, 6, and 9, centered at 91.5, 231, and 671 GHz, respectively. To mimic the realistic data format, we simulated nine channels around each central frequency with a width of 0.1 GHz. The intensity and corresponding optical depth profiles are presented in Appendix B for reference. Then, the two-dimensional intensity distributions were calculated for a geometrically thin, axisymmetric disk with a position angle (PA) of 6°0 and an inclination of 6°0 using Equation (6). The distance to the source was set to the same as HD 169142 (114.9 pc; Gaia Collaboration et al. 2023).

The resulting image cubes were processed using the CASA task `simobserve` to generate interferometric visibilities. We adopted ALMA antenna configurations designed to achieve a spatial resolution of ∼50 mas: C43-10 and C43-7 for Band 3, C43-8 and C43-5 for Band 6, and C43-6 and C43-3 for Band 9. Integration times were set to 10,000 s for the long-baseline (LB) configurations and 2000 s for the short-baseline (SB) configurations. Thermal noise was added with the default setting of `simobserve`, where the precipitable water vapor is 0.5 mm and the ground ambient temperature is 270 K. We created two distinct datasets: an "SB + LB" set by concatenating both configurations, and an "SB-only" set using only the SB data.

Figure 2 presents the CLEAN images generated from these visibility cubes. For comparison, the images in each set were smoothed to a common beam that is circular when the images are deprojected (0″06 for SB + LB and 0″25 for SB-only data). The rms noise levels are 4.4, 7.0, and 110 μJy beam^{-1} for the Band 3, 6, and 9 images from the SB + LB data, respectively. The noise levels of the SB-only data are ∼3-5 times larger than the SB + LB data for each band. Even in the SB + LB data, the rings are not perfectly resolved due to the beam size (∼6 au at 114.9 pc). The SB-only data, hampered by lower resolution, totally fail to distinguish the closely spaced rings at $r \sim 0''5$, showing only two broad features.

3.2. Conventional Method

As a baseline for comparison, we first applied a conventional image-based analysis to the mock data. We azimuthally averaged the CLEAN images using the `GoFish` package (R. Teague 2019) to produce radial intensity profiles. The uncertainties included both the image noise and a flux scaling factor f, modeled as a lognormal distribution $f \sim \exp(\mathcal{N}(0, \sigma_f))$, where $\mathcal{N}(0, \sigma_f)$ represents the normal distribution with the mean of zero and standard deviation of σ_f. We adopted calibration uncertainties of $\sigma_f = 0.025$, 0.05, and 0.1 for Bands 3, 6, and 9, respectively.

At each radial bin, we fitted the SED model described in Section 2.2 and sampled the posterior distribution using the NUTS algorithm in `numpyro`. We utilized the same

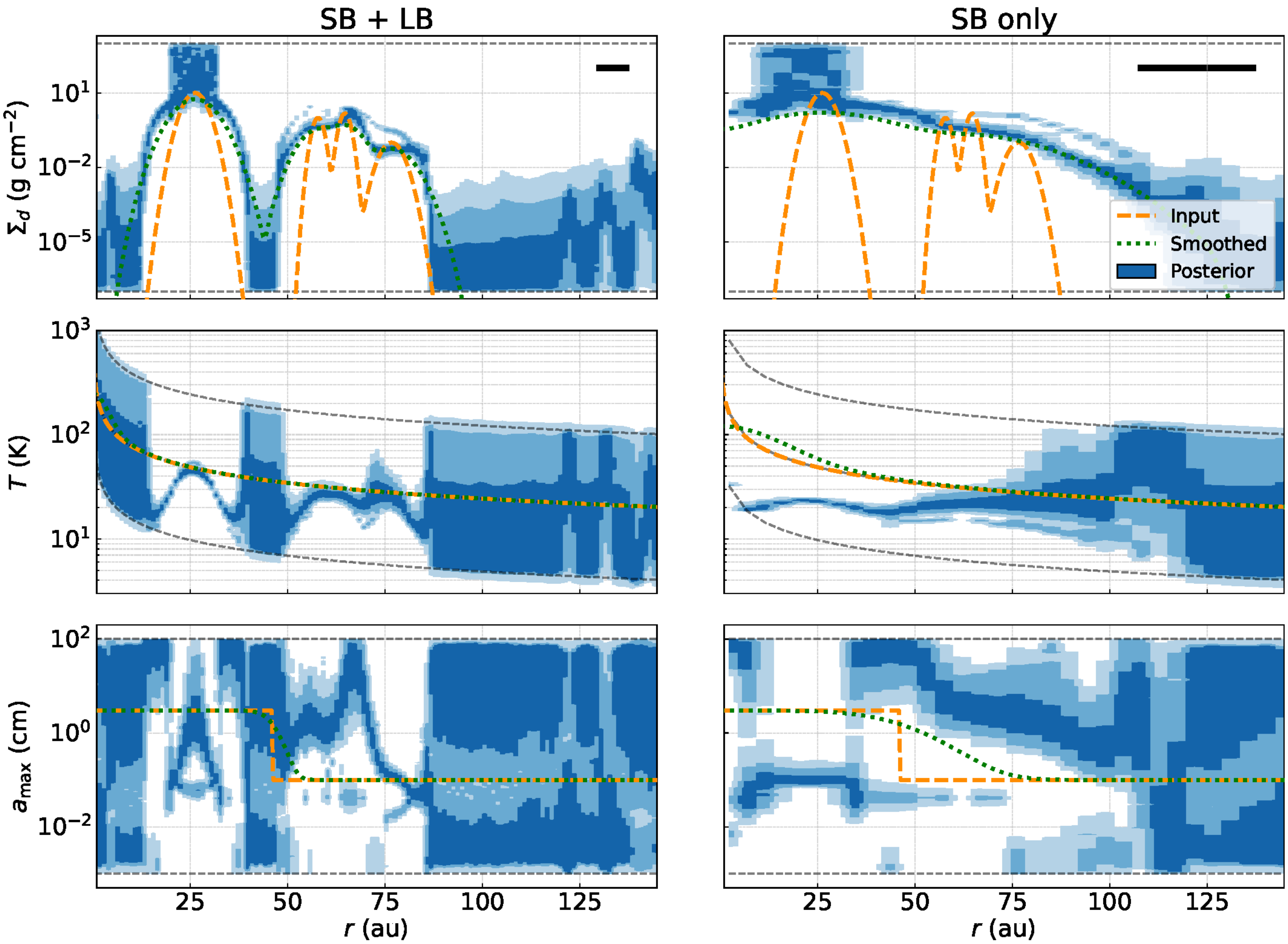

Figure 3. Marginal posterior distributions for the conventional image-based fitting. The orange dashed lines and green dotted lines represent the true input profiles and the profiles smoothed with the image beam sizes, respectively. The left and right columns show results for the SB + LB and SB-only datasets, respectively. Shaded regions indicate the 68.3%, 95.4%, and 99.7% (1σ, 2σ, and 3σ, respectively) highest-density intervals (HDIs). The black bars at the top indicate the FWHM of the synthesized beams.

DSHARP opacity model as used in the mock data generation. The free parameters were $\log_{10}\Sigma_d$, $\log_{10}T$, and $\log_{10}a_{\rm max}$, with $q = 3.5$ fixed. We employed uniform priors: $\log_{10}\Sigma_d \in [-7, 3]$ g cm^{-2}, $\log_{10}a_{\rm max} \in [-3, 2]$ cm, and a temperature range $[T_{\rm min}, T_{\rm max}]$ defined as 5 times lower and higher than the input profile (Equation (15)). The MCMC chains consisted of 2000 warm-up steps and 1000 sampling steps across 32 chains.

Figure 3 shows the resulting marginal posterior distributions. Comparison with the input profiles reveals several systematic biases. First, the spatial resolution of the CLEAN beam limits the ability to recover tightly packed ring structures. Second, beam smearing causes an overestimation of the surface density across most radii, although those are similar to the input profiles smoothed with the imaging beam sizes. Third, the inferred temperatures are biased toward lower values due to beam dilution of the emission peaks. Finally, the retrieved $a_{\rm max}$ values are almost always inaccurate, showing both over- and underestimations. Furthermore, these biases also depend on the spatial resolution; in the SB-only case, the effect is more severe than the SB + LB case. These results are basically consistent with a similar exercise by E. M. Viscardi et al. (2025).

To quantitatively estimate the uncertainty, we calculate the total dust mass for $r > 46$ au, where the surface density appears better constrained, from 10,000 random samples from each radius of the posterior. We present the posterior distribution in Appendix C. While the true input mass is $100\,M_\oplus$, the image-based fitting yields 200^{+25}_{-21} and $290^{+57}_{-38}\,M_\oplus$ for the SB + LB and SB-only datasets, respectively. This demonstrates that conventional methods can lead to a severe overestimation of the total dust budget in disks.

3.3. FRAP Fitting

3.3.1. Visibility Reduction

Using the same mock datasets, we evaluate the performance of our proposed method. In FRAP, we directly fit the one-dimensional visibility profiles. While it is possible to project each individual (u, v) point to its corresponding deprojected uv distance at each frequency, this needs expensive Hankel transform calculation for large datasets during posterior sampling. Therefore, in advance, we compress the data by calculating visibility values at a representative set of frequencies and uv distances.

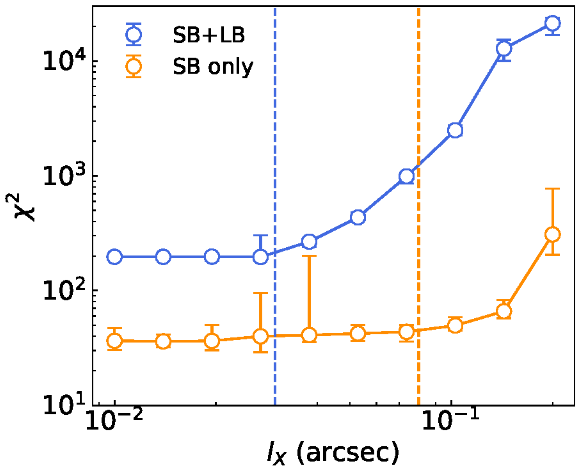

Figure 4. χ^2 values as a function of the GP length scale l_X from the cross-validation analysis. For the SB + LB data, χ^2 remains nearly constant for length scales $l_X < 0\farcs03$ (indicated by the blue dashed line), suggesting that models within this regime are equally consistent with the data.

First, the uv space in the wavelength unit is binned with a separation of

$$\Delta q_{\rm uv} = \frac{1}{\Theta}, \tag{17}$$

where we adopt $\Theta = 40''$ ($\simeq 1.9 \times 10^{-4}$ radians) to prevent aliasing effects (e.g., A. R. Thompson et al. 2017). Within each cell, the visibility points at (ν, $q_{\rm uv}$) are fitted using a first-order Taylor expansion:

$$\bar{\mathcal{V}}(\nu, q_{\rm uv}) = \bar{\mathcal{V}}_0 + \frac{\nu - \nu_0}{\nu_0} c_1 + \frac{q_{\rm uv} - q_{\rm uv,0}}{q_{\rm uv,0}} c_2, \tag{18}$$

where ν_0 is the representative frequency and $q_{\rm uv,0}$ is the center of the uv cell. The parameters $\bar{\mathcal{V}}_0$, c_1, and c_2 are free parameters in the local fit, where $\bar{\mathcal{V}}_0$ represents the representative visibility value at the cell center. This procedure is implemented using `scipy.optimize.curve_fit` (P. Virtanen et al. 2020) to obtain $\bar{\mathcal{V}}_0$ and its associated uncertainty across all uv cells. The fitting is performed for cells with nonzero visibility points. The reduction of visibility data is conducted for each band.

3.3.2. Sampling

We apply FRAP to the prepared one-dimensional visibilities, fixing $q = 3.5$ for direct comparison with the conventional method but keeping other parameters free. In Appendix D, we also demonstrate an additional fitting with q being a free parameter. We adopt 130 radial grid points extending to $R_{\rm out} = 1\farcs3$. As discussed in Section 2.1, the GP length scale l_X is an important hyperparameter that determines the smoothness of the retrieved profiles. To determine l_X in a data-driven manner, we perform a tenfold cross-validation analysis.

The data for each band are randomly partitioned into ten groups. We perform maximum a posteriori (MAP) estimation using stochastic variational inference on nine groups for a fixed l_X and calculate the resulting χ^2 against the remaining test group. This process is repeated for all groups to determine the median and 16th–84th percentiles of χ^2 for various values of l_X ($0\farcs01$–$0\farcs2$). As shown in Figure 4, χ^2 is nearly minimized and constant for $l_X \lesssim 0\farcs03$ in the SB + LB case, while it increases significantly for larger l_X. Consequently, we select $l_X = 0\farcs03$ for the SB + LB data and $l_X = 0\farcs08$ for the SB-only data. We discuss this selection in Section 3.3.4.

For the fixed hyperparameter, the prior distributions are visualized in Figure 5. The left panel shows individual sample paths drawn from the GP prior, illustrating the wide range of radial variations permitted by the framework. The black bar at the top-left panel indicates the adopted length scale ($l_X = 0\farcs03$). The right panel represents the same distributions using HDIs. For the sake of clarity, we adopt the HDI visualization for the remainder of this work.

We perform posterior sampling using MCMC and NUTS with 32 chains. Each chain consists of 5000 warm-up steps and 1000 sampling steps. The entire computation takes ~1 hr on a workstation equipped with an AMD EPYC 7343 processor. We note that the computation time significantly depends on the number of radial points.

Figure 6 displays the posterior distributions from the FRAP fitting. In contrast to the conventional image-based analysis, the results are much closer to the input profiles, suggesting that the method exhibits significantly reduced biases. Notably, in the SB + LB case, the tightly packed outer rings, which were unresolved in the CLEAN images, are successfully recovered in the surface density profile. There are deviations of the posterior median from the input surface density and temperature profiles at $r \sim 70$ au, however, they are reasonably covered by the uncertainty ranges. It is notable that the surface density posterior in the regions where the input value is almost zero ($r < 20$, ~50, and >100 au) gives the upper limits. Although the median values are higher than the lower boundary, this is mathematically natural and should not be considered as constraints, given that the lower sides of the posterior are just determined by the prior (Figure 5).

For the SB-only case, the adopted l_X is insufficient to express the actual radial variation of the surface density profile, resulting that the individual rings remain unresolved and the uncertainties are underestimated. Still, compared to the conventional method, the resulting profiles are much more closer to the input ones, which is a preferable feature. Furthermore, in both cases, the temperature is much better constrained, and the maximum dust size is also better behaved, compared to the conventional method.

In Appendix C, we present the posterior distribution of the dust mass at $r > 46$ au for a comparison with the conventional method (Section 3.3.2), suggesting that the total dust mass is also reasonably recovered.

3.3.3. A Case with Different Configurations among Bands

So far, we performed analysis for datasets with the same antenna configurations among bands. However, FRAP is not limited to this ideal case and treats different configurations at the same time. To demonstrate this, we perform the same injection–recovery test in Section 3 but change the combination of the configurations to (1) SB + LB for Bands 6 and 9, and the SB-only configuration for Band 3, and (2) SB + LB for Band 6, and the SB-only configuration for Bands 3 and 9.

In Figure 7, the results are presented. In both cases, the input profiles are well recovered. One difference is the uncertainty range; as information of the LB decreases, resultant uncertainty increases.

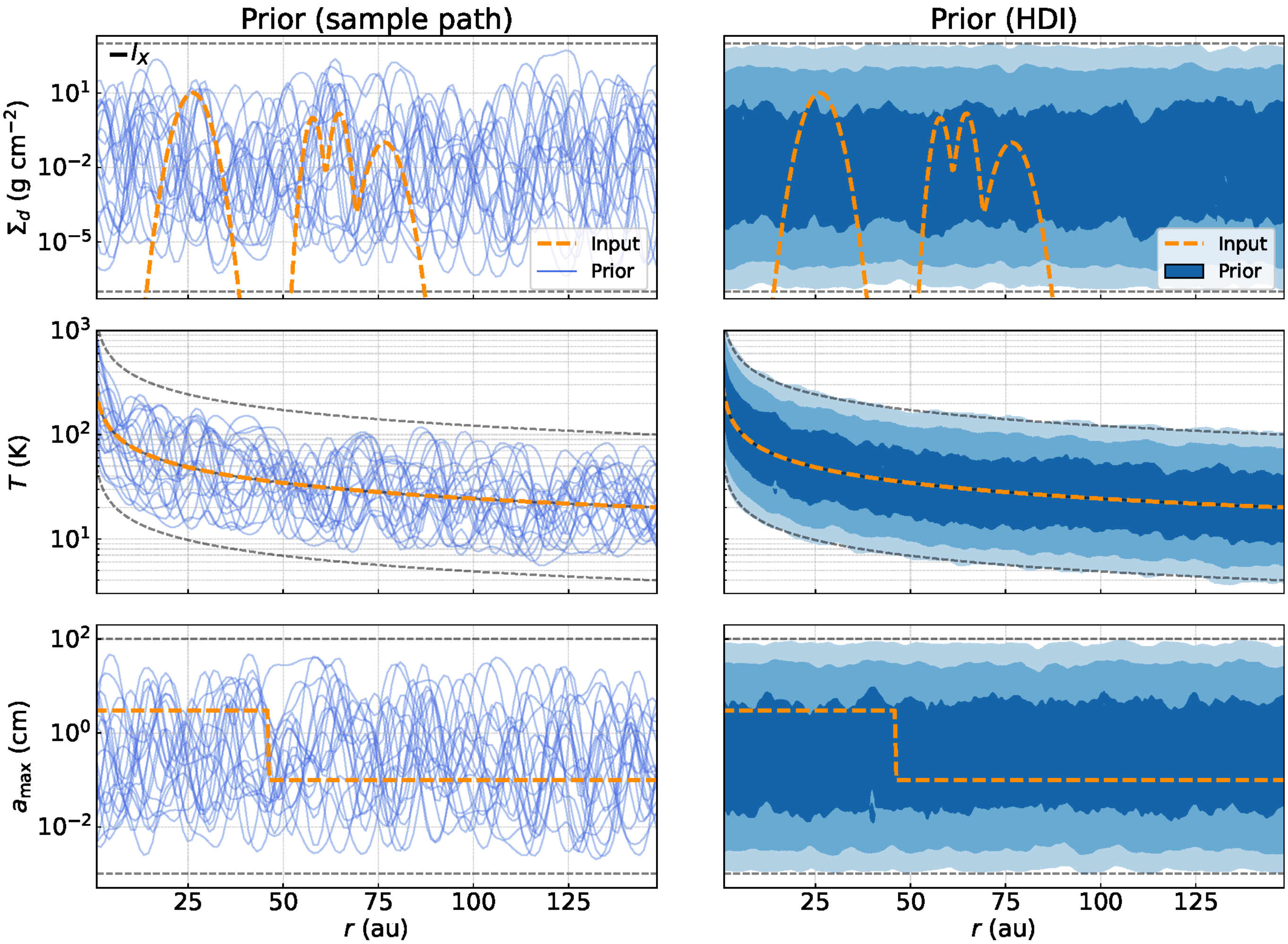

Figure 5. Left: 20 selected prior sample paths of the physical parameters used for the FRAP retrieval. The ensemble of paths demonstrates that the prior distribution sufficiently encompasses the true input profiles (orange dashed lines). The black bar in the top-left panel corresponds to the length scale $l_X = 0\rlap{.}''03$. Right: the same prior distribution visualized using HDIs. The three shaded regions indicate the 68.3%, 95.4%, and 99.7% (1σ, 2σ, and 3σ, respectively) HDI at each radius, respectively.

3.3.4. On the Selection of the Length Scale Parameter

To investigate the sensitivity of our results to the choice of l_X, we perform additional sampling with $l_X = 0\rlap{.}''01$ (Figure 8). For the SB + LB data, the results remain consistent with the input model, although the uncertainties are larger compared to the $l_X = 0\rlap{.}''03$ case. This increased uncertainty arises from the higher flexibility allowed by the smaller length scale, which permits small-scale oscillations. Crucially, however, the lack of strong bias remains. In the SB-only case, the higher flexibility allows that now the uncertainty range covers the input profiles. We plot additional examples with different l_X in Appendix E.

These examples show that increasing l_X affects the retrieved posteriors since variations on scales smaller than l_X are effectively smoothed. However, the results can only be significantly deviated from reality if the scale length is larger than the scale of the physical variation, which is happening in the SB-only case of Figure 6. In other cases, the results reasonably cover the truth within the uncertainty range, although the uncertainty itself depends on the length scale (i.e., smaller length scales make larger uncertainties).

This behavior could be leveraged by setting l_X based on physical motivations. For instance, one idea is setting l_X to the local gas scale height. Still, it would require sufficiently deep high-resolution observations for meaningful results. Therefore, in most cases, determining l_X via cross validation is sufficient, provided it is acknowledged that the model is insensitive to variations below this scale. We note that, while it is possible to treat l_X as a free parameter, which is a common practice in GP regression, the constant χ^2 values at small l_X (as seen in the cross validation; Figure 4) often make it difficult to derive meaningful constraints on l_X directly from the data.

4. Application to ALMA Observations of the HD 169142 Disk

In this section, we apply the developed framework to actual ALMA observations of the protoplanetary disk around HD 169142. HD 169142 is a Herbig Ae star located at a distance of 114.9 pc from the Earth (Gaia Collaboration et al. 2023) with a well-known protoplanetary disk. The dust component of the disk has been extensively studied across various wavelengths (M. Fukagawa et al. 2010; M. Honda et al. 2012; S. P. Quanz et al. 2013; M. Osorio et al. 2014; M. Momose et al. 2015; D. Fedele et al. 2017; E. Macías et al. 2019; S. Pérez et al. 2019; M. Lucas et al. 2025), consistently revealing that the disk consists of two major rings at ∼26 and

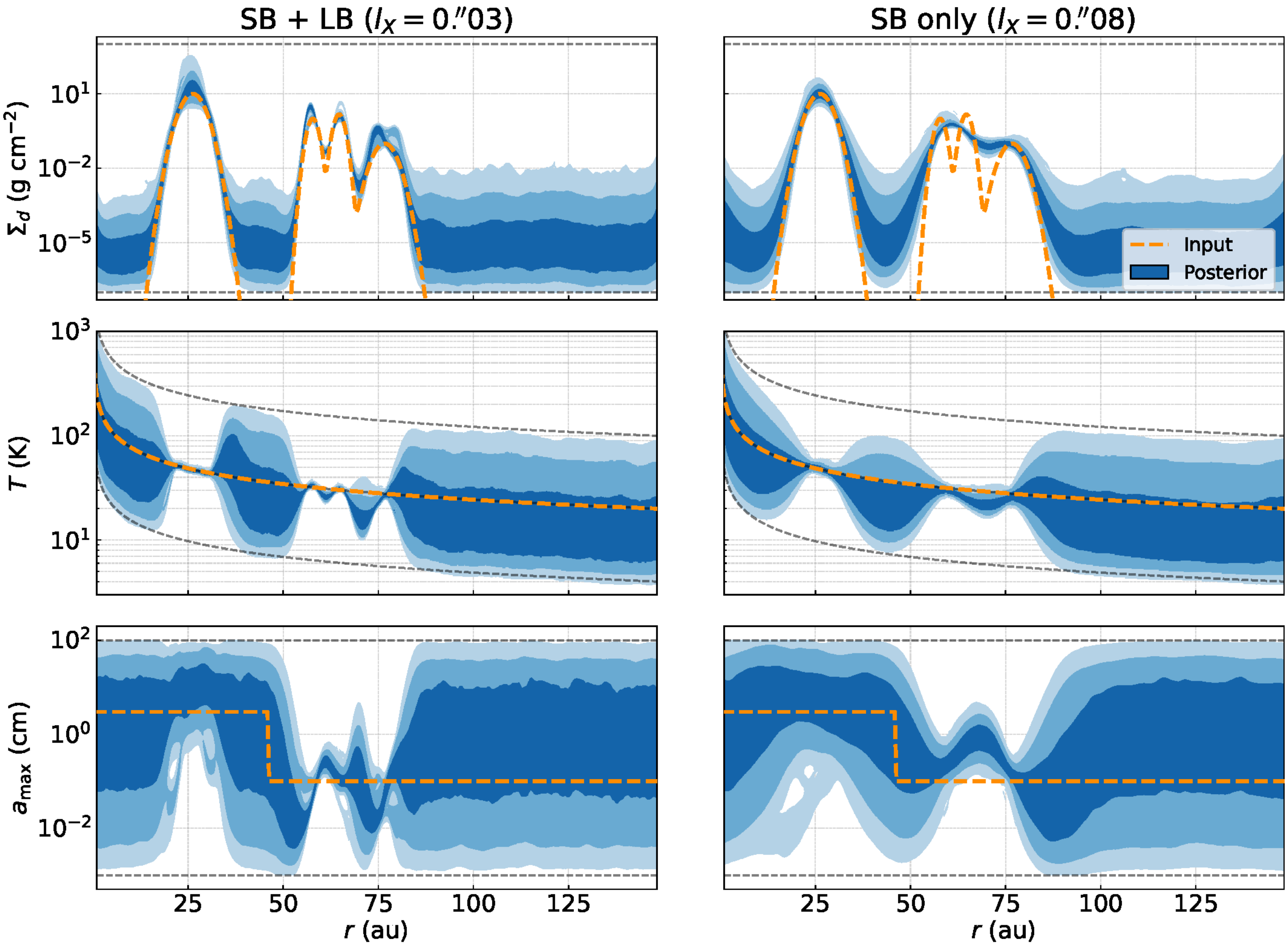

Figure 6. Marginal posterior distributions obtained with `FRAP`. Shaded regions indicate the 68.3%, 95.4%, and 99.7% (1σ, 2σ, and 3σ, respectively) HDIs. Compared to the conventional method (Figure 3), the results are significantly less biased and accurately recover the input parameters in both configurations.

~60 au from the central star. The highest spatial resolution observations to date further revealed that the outer ring is composed of at least three narrow (~5 au) rings (S. Pérez et al. 2019).

4.1. Observations and Data Reduction

We analyze multiband continuum data from ALMA Band 3 ($\lambda \sim 3.1$ mm), Band 6 ($\lambda \sim 1.3$ mm), and Band 9 ($\lambda \sim 0.45$ mm). The observational details are summarized in Appendix F. In the following, we describe the calibration and data reduction procedures.

4.1.1. Band 3

The Band 3 continuum observations ($\lambda = 3.1$ mm) were conducted under program #2018.1.01716.S (PI: E. Macías) and originally published by A. A. Rota et al. (2024). We retrieved the pipeline-calibrated measurement sets from the NRAO archive and performed additional self-calibration using the `exoALMA` pipeline (R. A. Loomis et al. 2025).

The self-calibration process involved six rounds of phase-only calibration for the SB data, with solution intervals ranging from the execution block (EB) length down to 10 s. After concatenating the SB data with the LB configurations, we performed six additional rounds of phase-only self-calibration and one final round of amplitude and phase calibration using the EB length as the interval. Although our analysis is primarily performed in the visibility domain, we generated a CLEAN image (`robust` = 0.0) for visualization, yielding a synthesized beam size of 41 × 38 mas (PA = 83°). To ensure a consistent multiwavelength comparison, the image was smoothed to a resolution that becomes a 45 mas circular beam when deprojected to a face-on geometry. The rms noise level of the smoothed image is 4.4 μJy beam^{-1}.

4.1.2. Band 6

For Band 6, we utilized archival data from four different projects. These datasets were selected based on the criterion that they cover the CO $J = 2$–1 line, the detailed analysis of which will be presented in a forthcoming paper (T. C. Yoshida et al. 2026, in preparation). Following the standard pipeline calibration for each dataset, we applied the `exoALMA` self-calibration pipeline to the concatenated continuum data. This process included four rounds of phase-only self-calibration for both the SB and LB data, with intervals decreasing to 60 s, followed by one round of amplitude and phase self-calibration. A CLEAN image was generated with `robust` = 0.0, resulting in a synthesized beam of 42 × 26 mas (PA = 73°). Similar to the Band 3 data, the image was smoothed to a deprojected

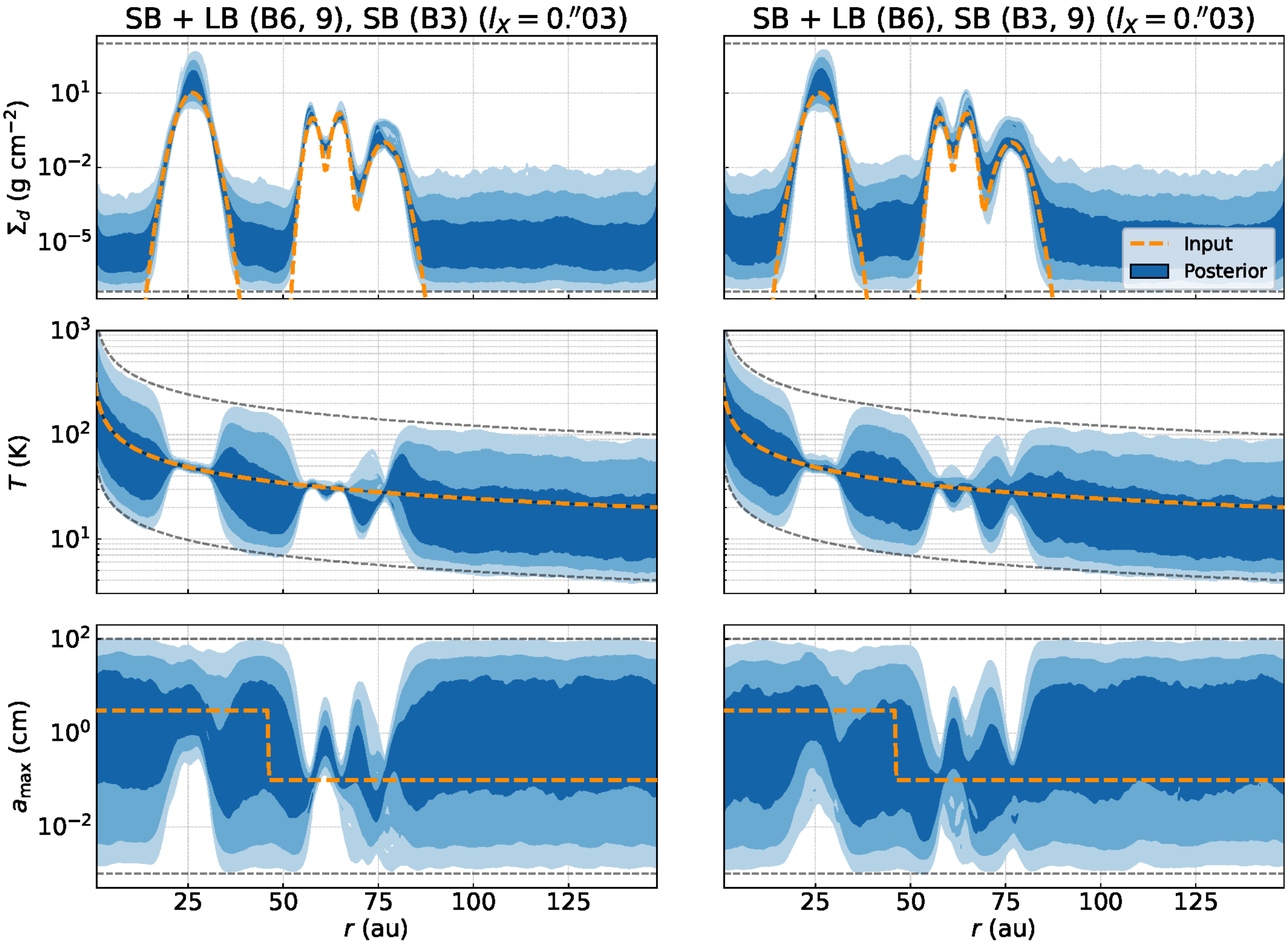

Figure 7. Marginal posterior distributions obtained with FRAP for the case with different configurations among bands. Shaded regions indicate the 68.3%, 95.4%, and 99.7% (1σ, 2σ, and 3σ, respectively) HDIs.

face-on resolution of 45 mas. The resulting rms noise level is 11.3 μJy beam^{-1}.

4.1.3. Band 9

For Band 9, we incorporated data from projects #2017.1.00727.S (PI: J. Szulágyi) and #2024.1.01254.S (PI: T. C. Yoshida). The former and later program correspond to the LB and SB, and the both originally consist of two EBs. However, we found that the second EB of the SB program was affected by significant phase decoherence, resulting in a large (a factor of 2) discrepancy in the total flux. Therefore, we decided to flag the second EB and only use the first EB. After pipeline calibration, the data were self-calibrated using the exoALMA pipeline. We performed seven rounds of phase-only self-calibration for the SB data, with intervals ranging from the EB length down to 10 s. This was followed by one round of amplitude and phase self-calibration using an EB-length interval to specifically calibrate the flux offsets between EBs. This calibrated SB dataset was then concatenated with the LB data, and the entire self-calibration procedure was repeated with an additional second round of amplitude and phase self-calibration using a scan-length interval. The final CLEAN image (robust = 0.5) has a synthesized beam of 35 × 32 mas (PA = 86°). After smoothing to the 45 mas beam, the rms noise level is estimated to be 0.20 mJy beam^{-1}.

4.2. Data-driven Estimation of Absolute Flux Uncertainty

Since the uncertainty in absolute flux calibration is a dominant factor in the total flux accuracy, a careful assessment is essential. While the ALMA Technical Handbook (P. Cortes et al. 2025) provides general stability guidelines for calibrators, actual uncertainties can vary significantly (L. Francis et al. 2020; T. C. Yoshida et al. 2025). Therefore, we estimate the flux uncertainty in a data-driven manner for each band.

First, we measure the flux ratios of each EB relative to a reference EB within the same band just after their phase-only self-calibration, utilizing azimuthally averaged visibility profiles as implemented in the exoALMA calibration script (S. M. Andrews et al. 2018; R. A. Loomis et al. 2025). The SB EB with the highest signal-to-noise ratio is selected as the reference, consistent with our self-calibration procedure. We then group these ratios for EBs observed within a 30 day window, representing the typical duration of an observing project, and calculate the mean for each group.

The final mean flux scaling factor for a given band, $\bar{f}$, is obtained by averaging the mean values across all groups. The associated uncertainty is estimated as

$$\sigma_{\bar{f}} = \frac{\max(\sigma_{\rm g}, \sigma_n)}{\sqrt{N_{\rm b}}}, \tag{19}$$

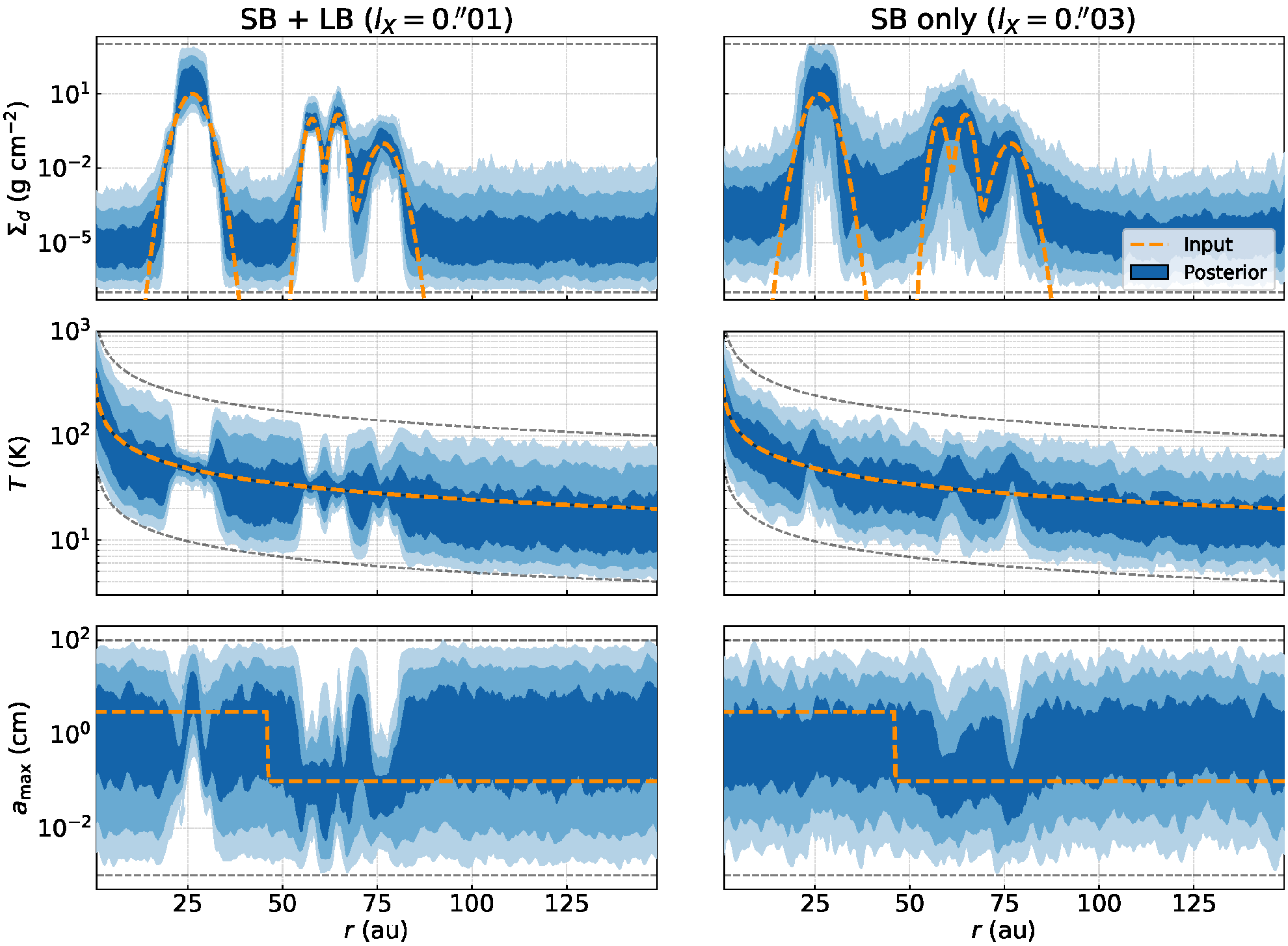

Figure 8. Marginal posterior distributions for additional sampling with alternative length scales ($l_X = 0.''01$).

where σ_g is the standard deviation of the group averages, σ_n is the nominal accuracy reported in the ALMA Technical Handbook ($\sigma_n = 0.025$, 0.05, and 0.2 for Bands 3, 6, and 9, respectively), and N_b is the number of independent groups in the band.

The resulting mean values and standard deviations are summarized in Table 1. We note that $\bar{f}$ serves as a nuisance parameter, as its absolute value depends on the choice of the reference EB. We confirmed that these results are not very sensitive to the grouping duration. These empirically derived values are adopted for the subsequent retrieval analysis.

Table 1
Absolute Flux Uncertainties Derived from the Observational Data

Band	$\bar{f}$	$\sigma_{\bar{f}}$	σ_n
3	1.0	0.018	0.025
6	1.1	0.063	0.050
9	0.98	0.14	0.20

4.3. Constraining Disk Geometry

Since FRAP operates on visibility data reduced to one-dimensional radial profiles, the disk geometry must be accurately constrained beforehand. We employ the protomidpy package (M. Aizawa et al. 2024) to fit axisymmetric intensity models to the two-dimensional visibilities. This allows us to constrain the disk center coordinates, inclination i, and PA independently for each band.

After identifying the geometric parameters, we align the disk center with the phase center using the CASA task fixvis. For the final visibility deprojection and azimuthal averaging, we adopt the inclination and PA derived from the Band 6 data ($i = 6.^{\circ}3$ and PA $= 6.^{\circ}3$; coincidentally the same numbers), which provided the highest signal-to-noise ratio among the available datasets.

4.4. Overview of the Images and Radial Profiles

Figure 9 displays the resulting CLEAN images of the processed datasets. To facilitate a consistent multiwavelength comparison, all images were smoothed to a common effective resolution of 45 mas after deprojecting to a face-on geometry. Figure 10 provides zoom-in views of the innermost regions, confirming that the central disk component is detected across all observed bands.

While the continuum images exhibit several asymmetric features that have been discussed in previous studies (S. Pérez et al. 2019; M. Lucas et al. 2025), this work focuses on the azimuthally averaged radial properties. Figure 11 shows the radial brightness temperature profiles in the Rayleigh–Jeans approximation extracted from the CLEAN images. We find

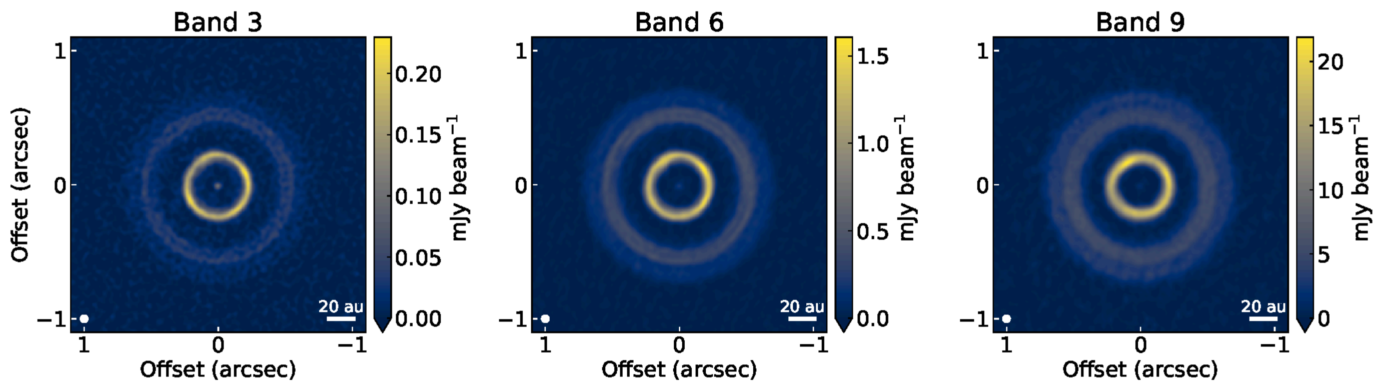

Figure 9. CLEAN images of the HD 169142 disk across three ALMA bands. The white ellipses at the bottom left indicate the synthesized beam size (45 mas). The white bars represent a scale of 20 au. Note that the images are not deprojected.

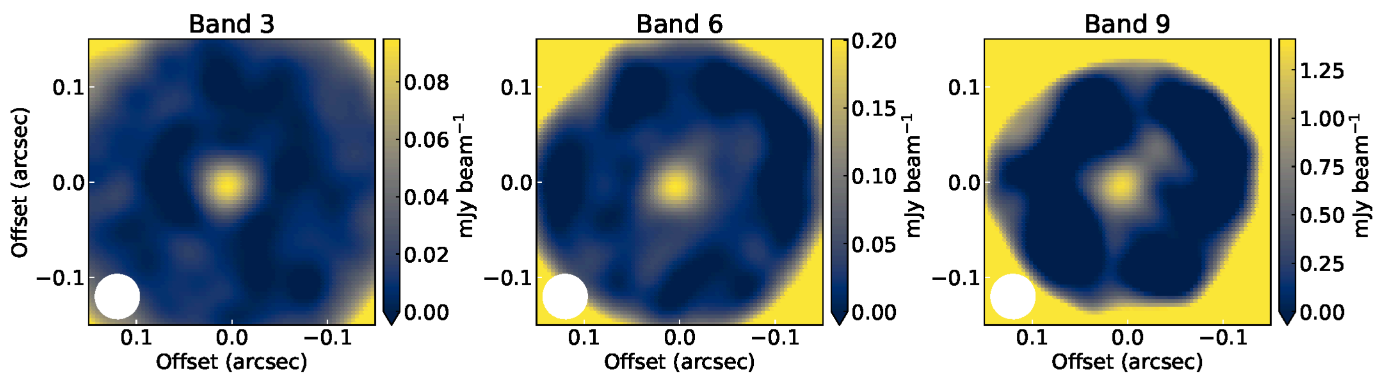

Figure 10. Zoom-in views of the innermost regions of the HD 169142 disk corresponding to the images in Figure 9.

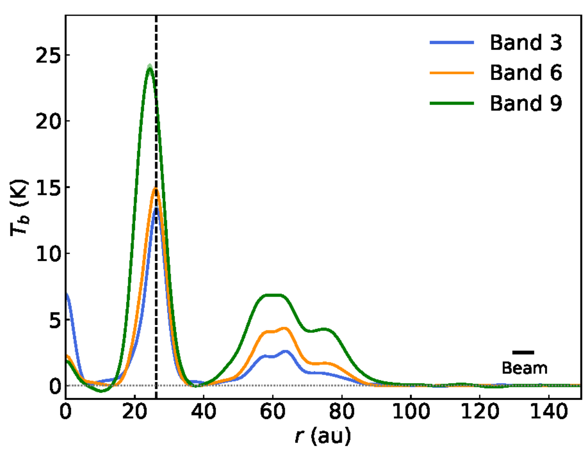

Figure 11. Radial brightness temperature profiles of the HD 169142 disk derived from the CLEAN images. The vertical dashed line indicates the peak location of the inner ring in Band 6 (∼26 au).

that the peak of the inner ring at ∼26 au in Band 9 is located at a slightly smaller radius compared to its counterparts in Bands 3 and 6. Furthermore, the inner ring in Band 9 appears substantially broader, and the outer disk emission is smoother than in the other bands. These morphological differences are potentially indicative of differential dust trapping and grain growth as a function of radius (e.g., K. Doi & A. Kataoka 2023), and/or an exposed edge of the ring from the central star with a high optical depth in Band 9.

In the innermost region ($r < 10$ au), a compact source is detected in all bands. While the brightness temperatures in Bands 6 and 9 are comparable, the brightness temperature in Band 3 is significantly higher. This relative enhancement at longer wavelengths suggests that an emission mechanism other than thermal-dust emission, such as free–free emission from ionized gas, contributes to the Band 3 flux in the central region.

4.5. Retrieving Dust Properties with FRAP

The retrieval procedure for the observational data follows the methodology validated through the mock tests (Section 3). We generated one-dimensional visibility profiles. For Band 3, however, we adopted two representative frequencies corresponding to the lower and upper sidebands. This accounts for the significant fractional band width of Band 3, where a single-frequency approximation may not sufficiently capture the spectral slope of the emission. The resulting visibility profiles are shown in Figure 12.

In this retrieval, we expand the parameter space by treating the power-law index of the dust grain size distribution, q, as a free parameter, in addition to the dust surface density ($\log_{10}\Sigma_d$), dust temperature ($\log_{10} T$), and maximum grain size ($\log_{10} a_{\max}$). We also test this problem setting using the mock datasets in Appendix D. We adopt the same prior boundaries as used in the mock tests, with the index q constrained between one and five. Based on a dedicated cross-validation analysis for this dataset, we selected a GP length scale of $l_X = 0\overset{''}{.}03$.

To assess the systematic uncertainties arising from dust property assumptions, we performed the retrieval using two distinct opacity models: the DSHARP model (T. Birnstiel et al. 2018) and the model presented by L. Ricci et al. (2010; assuming zero porosity). Both opacity tables were generated using the `dsharp_opac` module (T. Birnstiel et al. 2018).

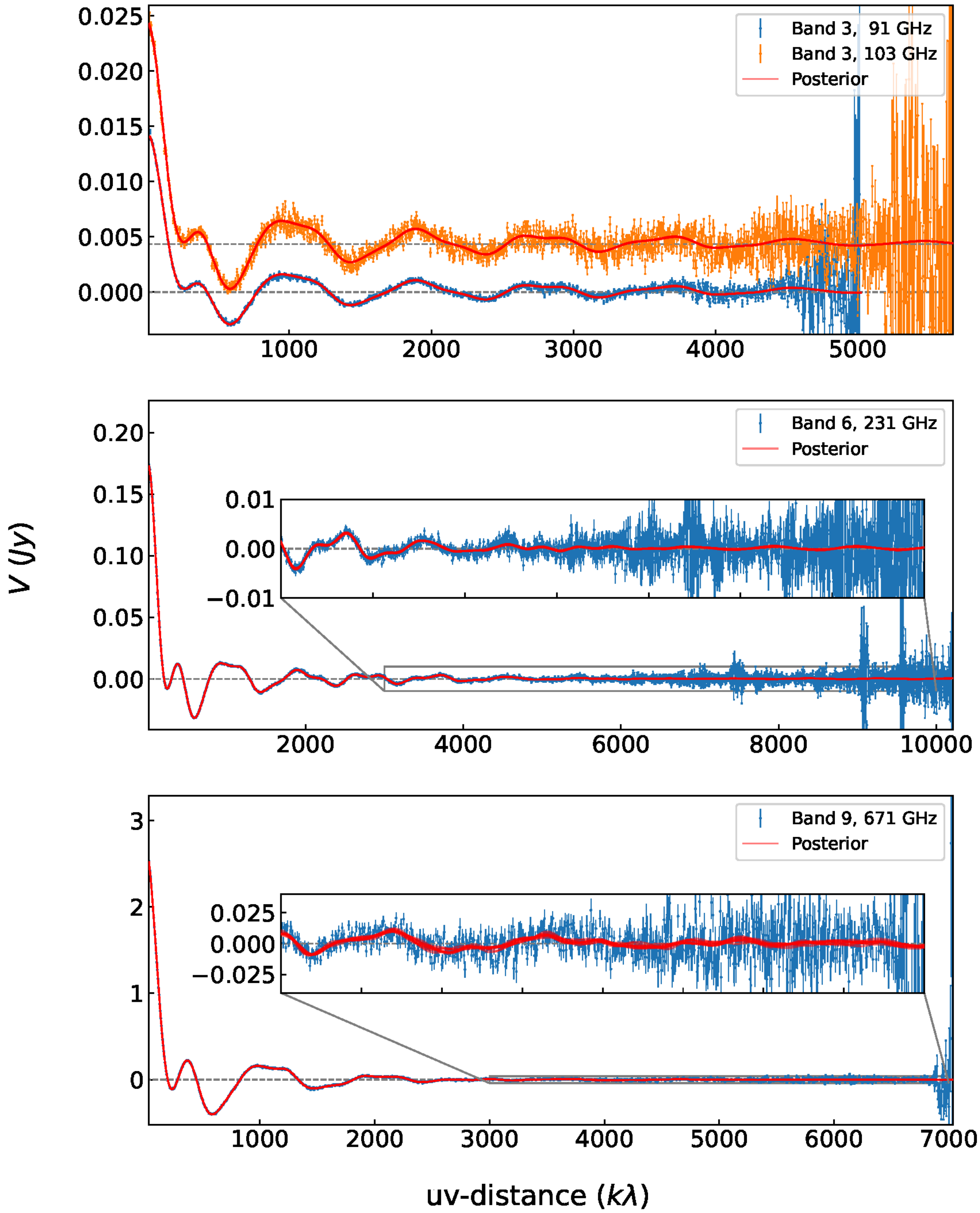

Figure 12. Visibility profiles of the HD 169142 disk across three ALMA bands. The data points include 1σ error bars. The solid red lines represent 10 randomly selected posterior samples from the FRAP fitting using the L. Ricci et al. (2010) opacity model, demonstrating the excellent agreement between the model and the interferometric data.

The central region of HD 169142 harbors a compact point source that may include contributions from free–free emission from ionized gas, as suggested by previous studies (E. Macías et al. 2017; A. A. Rota et al. 2024). To account for this without making assumptions about its physical origin, we incorporate an additional point-source component into the visibility model:

$$F_{\rm pt}(\nu) = F_0\left(\frac{\nu}{100\ \rm GHz}\right)^{\beta}, \tag{20}$$

where F_0 and β are the flux at $\nu = 100$ GHz and spectral slope, respectively. As priors, we set broad Gaussian distributions for these two parameters, $\log_{10}(F_0/\rm mJy) \sim \mathcal{N}(-1.0, 1.0)$ and $\beta \sim \mathcal{N}(0.0, 4.0)$. This power-law term represents the non-thermal-dust contribution at the disk center, effectively allowing the framework to isolate the thermal-dust emission from the total flux. We utilized the flux scaling uncertainties derived in Section 4.1. The posterior distribution was sampled using 10,000 warm-up steps and 1000 sampling steps across 32 chains. After sampling, for both opacity models, we identified that one chain was trapped in a region where the log probability is $\sim$1000 lower than that of the other chains. To ensure a proper evaluation of the posterior, this chain was excluded from the subsequent analysis as this behavior is purely a numerical artifact.

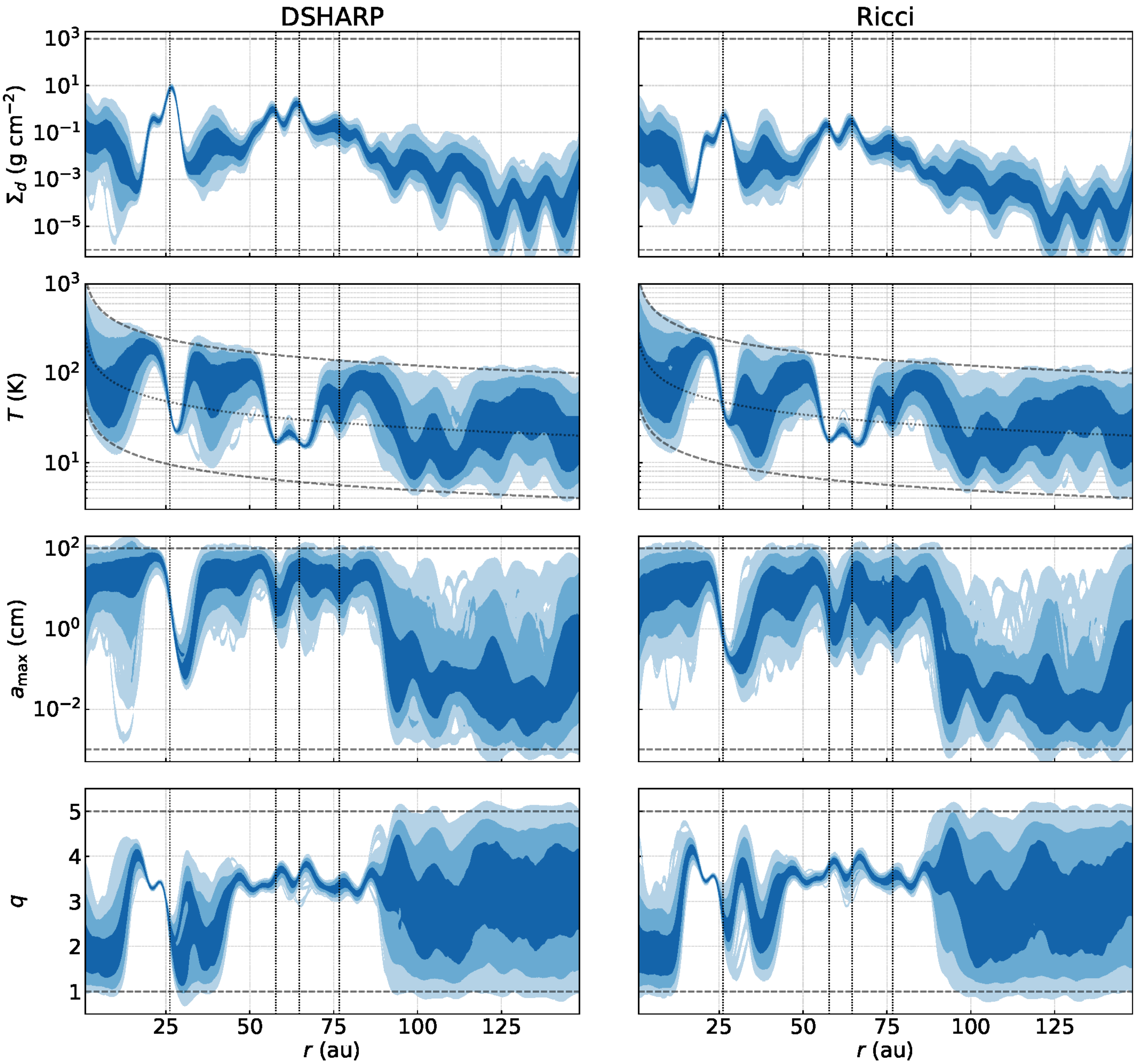

Figure 13. Marginal posterior distributions for the physical properties of the HD 169142 disk. Shaded regions indicate the 68.3%, 95.4%, and 99.7% (1σ, 2σ, and 3σ, respectively) HDIs. Results are compared between the DSHARP (left) and L. Ricci et al. (2010, right) opacity models. Black dashed lines indicate the prior boundaries. Vertical lines show the ring locations previously specified. Black dotted lines in the T panels show the temperatures expected from a passive disk model (Equation (15)).

4.6. Results

In Figure 12, the 10 randomly selected visibility profiles from the posterior distribution with the L. Ricci et al. (2010) opacity model are plotted, demonstrating that they are in excellent agreement with the interferometric data across all bands.

The retrieved physical quantities are presented in Figure 13. Our framework successfully reconstructs the radial profiles for both opacity models. The dust surface density profiles reveal a complex structure consisting of an inner ring at $\sim$26 au, three outer rings around $\sim$60 au (see also the intensity profiles in Figure 11), and a broad background extending up to $\sim$120 au. Notably, the surface density remains nonnegligible (10^{-3}–10^{-2} g cm^{-2}) even within the major gaps at $\sim$10 and $\sim$40 au, as well as in the regions beyond the primary rings. These posteriors are clearly distinct from those in the injection–recovery test, where a zero-input surface density yields a posterior consistent with the prior plus an upper limit (Section 3.3.2). Furthermore, the results indicate a significant contribution from dust grains in the innermost disk ($r < 10$ au). While the two opacity models yield structurally similar profiles, the absolute values of the surface density are generally lower in the L. Ricci et al. (2010) model. For reference, Figure 14 provides a linear-scale representation of the surface density profiles, which more clearly highlights the dominance of the multiple ring structures. The total dust mass is estimated to be 330^{+40}_{-30} and $49^{+7}_{-6}\,M_\oplus$ for the DSHARP and L. Ricci et al. (2010) opacities, respectively, with Gaussian-

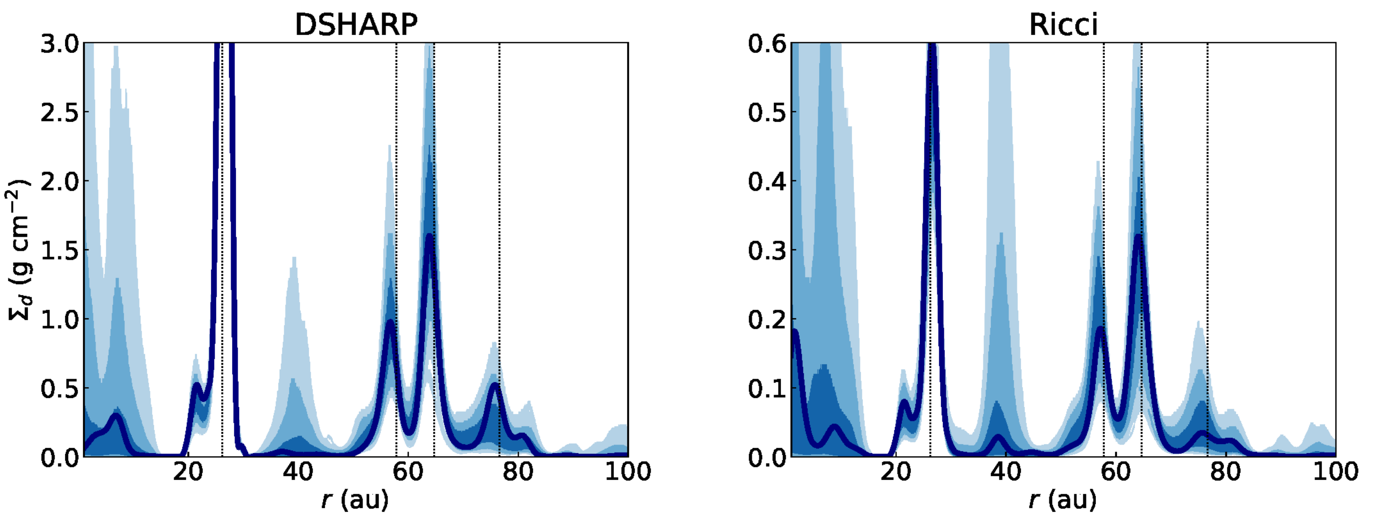

Figure 14. Marginal posterior distributions for the dust surface densities shown on a linear scale. Results are shown for the DSHARP (left) and L. Ricci et al. (2010, right) opacity models. Solid lines indicate the MAP samples.

like marginal posterior distributions. This discrepancy between two models is primarily because of the higher opacity of the L. Ricci et al. (2010) model.

The temperature profiles are well constrained primarily within the ring regions. A steep radial temperature gradient is suggested just inward of the 26 au ring. At the peaks of both the inner and outer rings, the retrieved temperatures are consistent with, or slightly lower than, the values expected from a standard passive disk model (dotted line in Figure 13; Equation (15)).

The maximum grain size at the inner ring is estimated to be $\sim$1 cm. In contrast, the outer rings and the innermost disk exhibit a lower limit of approximately $\sim$1 mm. Beyond the outer rings, the grain size appears to decrease toward $\sim$0.1 mm, although the uncertainties in this region are considerable. The power-law index q of the grain size distribution is largely consistent with the interstellar medium (ISM) value of 3.5 across most radii. While the DSHARP model allows for values as low as $q \sim 2$ at certain radii, this trend is not observed when the L. Ricci et al. (2010) model is adopted.

In Figure 15, we show the corresponding optical depth distributions at each band. The peak optical depth at the inner ring is $\sim$2, therefore, the intensity still has a sensitivity to the optical depth. The outer rings are essentially optically thin in all bands. Both opacity models suggest well-consistent results because the optical depths can be determined from data without assuming an opacity.

Figure 16 displays the spectra for the central region ($r < 45$ mas), distinguishing between the retrieved nonthermal-dust point source and the thermal-dust emission from the innermost disk, based on the L. Ricci et al. (2010) opacity results. We also overplot previous image-based flux measurements (E. Macías et al. 2017; A. A. Rota et al. 2024) and our own aperture photometry. The data strongly suggest that the Band 3 flux originates primarily from the additional nonthermal-dust component rather than thermal dust. This additional component exhibits a substantially flatter spectral slope compared to the thermal-dust emission. These spectral characteristics remain consistent regardless of the chosen opacity model.

Finally, the posterior distributions for the flux scaling parameters are shown in Figure 17. While the priors are centered on the observed values, the DSHARP model favors lower scaling factors, whereas the L. Ricci et al. (2010) model remains closer to unity. Although both models provide reasonable fits to the data after adjusting for flux calibration, the closer alignment of the L. Ricci et al. (2010) model with the nominal calibration suggests it may be more consistent with the observations.

5. Discussion

5.1. Comparison of FRAP to Other Approaches

In Section 3, we demonstrated that FRAP provides significantly less biased estimates of dust properties compared to the conventional radius-by-radius fitting approach. This advantage stems primarily from the high radial flexibility of our framework, whereas the conventional approach is fundamentally limited by the spatial resolution of the CLEAN beam. In this sense, FRAP achieves "superresolution," thereby maximizing the scientific potential of ALMA datasets.

It is instructive to compare our approach with other existing methods. frankenstein (J. Jennings et al. 2020) is a pioneering and widely used tool for reconstructing radial intensity profiles using GPs. While FRAP also utilizes a GP-based framework, a key difference exists. frankenstein regularizes the solution by assuming that the power of visibilities at unmeasured uv distances is essentially zero, and derives the radial intensity profile. On the other hand, FRAP regularizes the solution by assuming that the physical quantities, such as dust surface densities, are smooth, and directly derives the profiles of the physical quantities. To do so, FRAP is built upon a physical SED model that enables the simultaneous fitting of multiple frequencies. While our method is sensitive to the accuracy of the assumed physical model, this is a necessary trade-off that allows us to leverage physical constraints to better regularize the problem.

This physically motivated modeling is one of the cornerstones of our superresolution capability, although the visibility-based analysis itself can already achieve a super-CLEAN beam resolution (J. Jennings et al. 2020). A conceptual analogy can be found in stellar observations: while a single

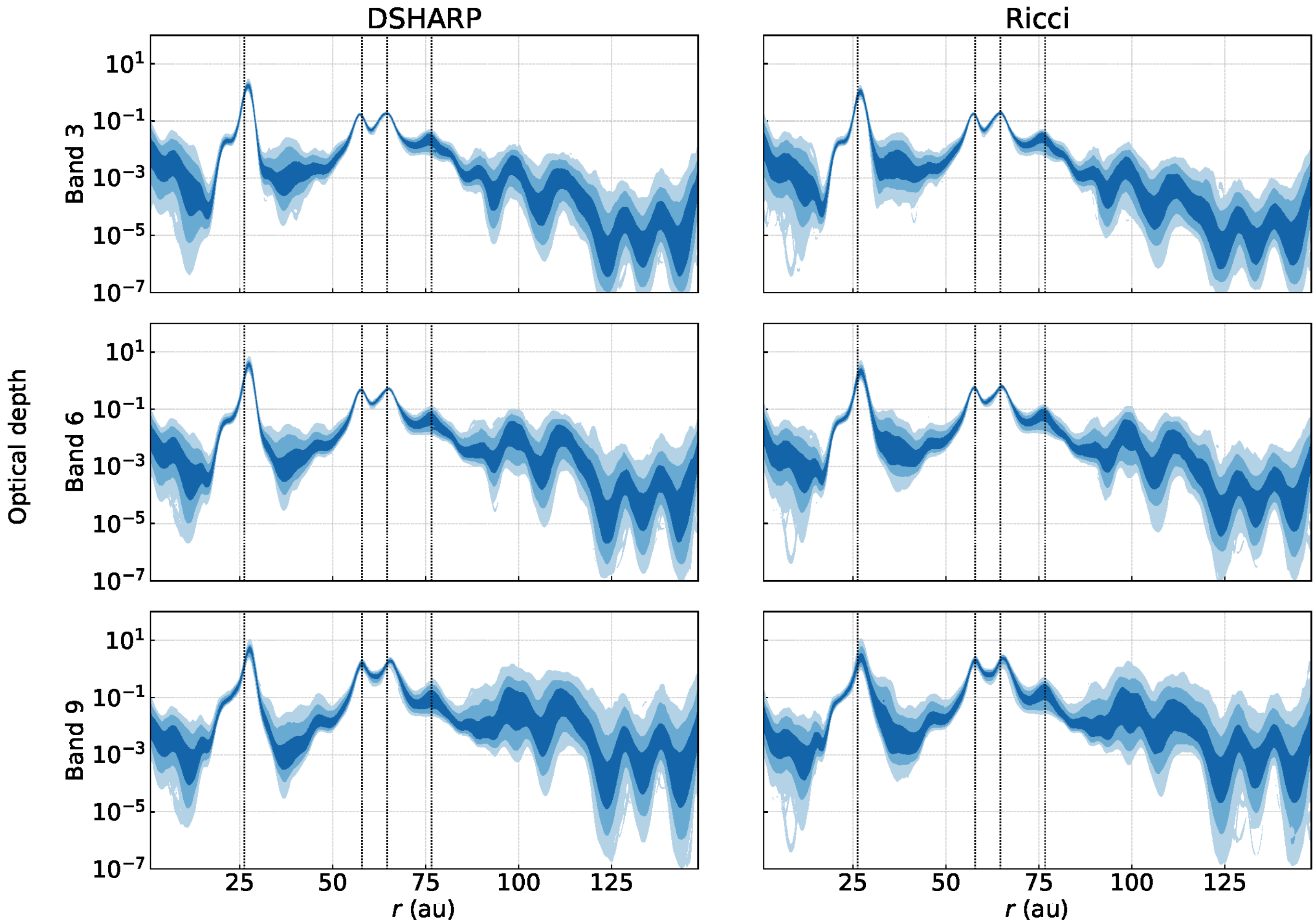

Figure 15. Marginal posterior distributions for the optical depths at each band. Shaded regions indicate the 68.3%, 95.4%, and 99.7% (1σ, 2σ, and 3σ, respectively) HDIs. Results are compared between the DSHARP (left) and L. Ricci et al. (2010, right) opacity models. Vertical lines show the ring locations previously specified.

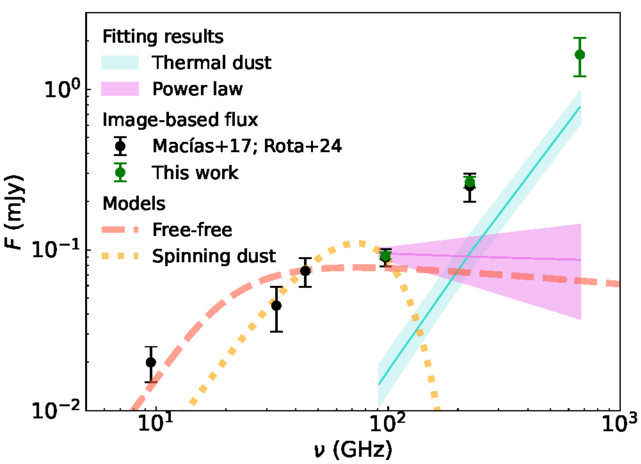

Figure 16. SED of the innermost region (r < 45 mas) and comparison with theoretical models for the L. Ricci et al. (2010) opacity case. Blue and magenta lines represent the retrieved SED for the thermal-dust and additional power-law components, respectively. Black and green points show image-based flux estimates from E. Macías et al. (2017) and A. A. Rota et al. (2024), and this work, respectively. The free–free emission and spinning dust models are indicated by the red dashed and orange dotted lines, respectively.

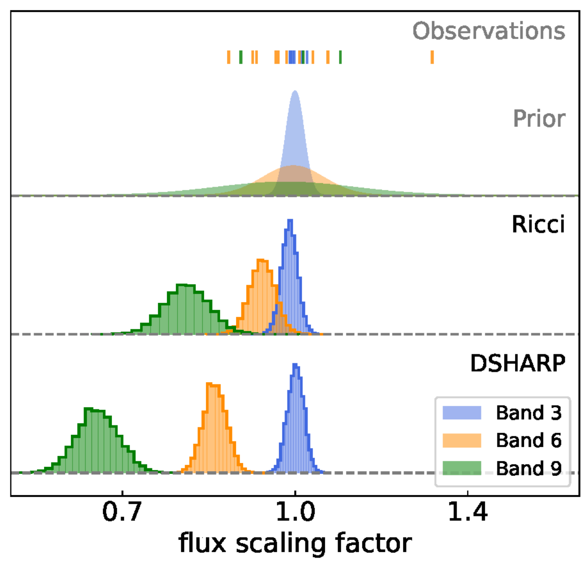

Figure 17. Prior and posterior distributions of the flux scaling parameters for each dataset.

telescope cannot resolve the surface of a distant star, its radius can be accurately estimated from its SED by applying appropriate stellar models. Similarly, even when rings and gaps in a protoplanetary disk are not spatially resolved, their underlying physical properties can be inferred by combining multiwavelength interferometric data with radiative transfer models.

Our approach shares some similarities with forward-modeling techniques that assume specific functional forms for the intensity profiles (e.g., E. Macías et al. 2019). However, FRAP only assumes that the radial variations are relatively smooth and can be described by a GP. This makes our framework significantly more flexible and less prone to the biases inherent in parametric models. Furthermore, the implementation of FRAP in JAX allows for auto-differentiation and accelerated sampling, enabling a robust Bayesian posterior estimation rather than a simple point estimate. This essentially addresses the overfitting issue that creates artifacts, making the method more reliable.

5.2. Limitations of FRAP

As discussed in Section 5.1, the primary limitation of FRAP lies in its dependence on model assumptions. In this study, we utilized the radiative transfer model described in Section 2.2. Exploring alternative models, such as those including vertical structure or more complex dust settling, would be beneficial for assessing how results vary under different physical conditions. It is also important that FRAP modeling assumes the disk is essentially axisymmetric.

Additionally, as discussed in Section 3.3.4, it is notable that the results depend on choice of the scale length, which essentially determines the flexibility of the model.

Regarding dust opacities, we compared two distinct models in Section 4. Such comparisons are essential to avoid underestimating the total uncertainty in the retrieved parameters. Moreover, our framework can potentially serve as a tool to evaluate the validity of various dust opacity models themselves (e.g., F. Zagaria et al. 2025).

The computational cost of FRAP is relatively modest when the GP hyperparameters are fixed (∼40 minutes for the demonstration in Section 3). However, the execution time increases significantly if these hyperparameters are treated as free parameters or if the number of radial sampling points is substantially increased.

5.3. Physical Implications for the HD 169142 Disk

5.3.1. Global Disk Structure

Previous studies (e.g., D. Fedele et al. 2017; E. Macías et al. 2019; S. Pérez et al. 2019) have established the presence of two primary dust rings in HD 169142, with the outer ring resolved into three tightly packed subrings. Our reconstructed profiles are broadly consistent with these findings while providing several new insights.

The inner ring at $r \sim 26$ au is not perfectly Gaussian-like but exhibits an "inner shoulder" in the dust surface density (Figures 13 and 14), a feature previously pointed out by S. Pérez et al. (2019). Similar asymmetric ring profiles have been observed in other disks (e.g., M. Benisty et al. 2021; K. Doi et al. 2024) and may be explained by leaky dust traps, where small grains drift inward from the main trap (P. Pinilla et al. 2024). The apparent inward shift of the ring peak in Band 9 (Figure 11) likely reflects this size-dependent distribution. Notably, M. Lucas et al. (2025) found the ring peak at ∼21 au in infrared scattered light compared to ∼27 au in Band 6, attributing this to a leaky trap. Our Band 9 peak at $r = 24$ au fits well within this sequence, tracing grains smaller than those at Band 6 but larger than those seen in the infrared.

In the outer disk, our results suggest that the relative surface densities of the three subrings depend significantly on the choice of dust opacity model. Hydrodynamic simulations by S. Pérez et al. (2019) suggest that the relative surface density of these rings may evolve over time, assuming they were formed by an embedded mini-Neptune-sized planet. Future comparisons between our retrieved surface densities and hydrodynamic models will be crucial for constraining these formation mechanisms.

The posterior distributions (Figure 13) indicate that the dust surface densities within the gaps at ∼20 and ∼40 au are nonnegligible. This supports the leaky trap scenario, where small grains cross the traps. While these grains are expected to be significantly smaller than those in the rings, current sensitivity limits preclude a precise measurement of grain sizes within the gaps.

Beyond the rings ($80 < r < 120$ au), we detect a diffuse outer disk with nonnegligible surface density, roughly coincident with the $C^{18}O$ emission extent (H. Garg et al. 2022). The median dust size profile shows a sharp transition at $r \sim 80$ au toward smaller grains (∼0.1–1 mm). This extended, small-grain disk is consistent with the analysis of the TW Hya disk (J. D. Ilee et al. 2022) and the predictions of G. P. Rosotti et al. (2019), suggesting that previous measurements of continuum disk radii were primarily sensitivity limited.

The total dust mass of ∼280 and ∼45 $M_\oplus$ for the DSHARP and L. Ricci et al. (2010) opacities, respectively, are also broadly consistent with the results by E. Macías et al. (2019), $160^{+250}_{-90}\,M_\oplus$, who performed a parametric model fitting.

The temperature profiles reveal a sharp drop inward of the inner ring at 26 au, with a similar, albeit less pronounced, trend at the inner edge of the outer rings. This likely reflects efficient heating at the illuminated inner edges of the rings (e.g., S. Bruderer 2013), consistent with infrared observations suggesting these rings are directly irradiated by the central star (I. Hammond et al. 2023; M. Lucas et al. 2025). In the inner side of the exposed cavity wall, the temperature exceeds ∼100 K, which is consistent with the brightness temperature of the CO line (M. Leemker et al. 2022). Furthermore, such high temperature may lead to the sublimation of water ice. Indeed, A. S. Booth et al. (2023) detected molecules that should be enhanced at the water snow line, methanol and SO, at this radius. The correspondence of the water snow line and exposed inner cavity wall has been also found in the HD 100546 disk (L. Rampinelli et al. 2026).

Finally, we find that the power-law index of the grain size distribution is remarkably consistent with $q \sim 3.5$, the ISM value (J. S. Mathis et al. 1977), across the disk. In well-structured disks where grain growth is expected, a value of $q \sim 3.5$ often points to a steady-state collisional cascade, where the size distribution is maintained by the fragmentation of larger bodies (J. S. Dohnanyi 1969; H. Tanaka et al. 1996; T. Birnstiel et al. 2011).

5.3.2. Innermost Disk

We retrieved the spectrum of the innermost disk at $r < 10$ au simultaneously with the outer disk (Figure 16), where the nonthermal-dust component exhibits a very shallow or even negative spectral index. At wavelengths longer than Band 3, bright emission has been detected in this same region (E. Macías et al. 2017; A. A. Rota et al. 2024). To explain such long-wavelength emission near a disk center, free–free emission is a well-considered mechanism (e.g., A. A. Rota et al. 2024). Another possibility would be emission from spinning dust grains (C. Dickinson et al. 2018). These spectra often degenerate at frequencies $\nu < 100$ GHz. Indeed, T. Hoang et al. (2018) proposed that a spinning dust spectrum fits the spatially integrated SED of the HD 169142 disk, while A. A. Rota et al. (2024) suggested free–free emission based on a tight correlation between the emission and the stellar accretion rate across a large sample including HD 169142.

The degeneracy, however, can be broken by observing the flux at higher frequencies; spinning dust emission exhibits a sharp drop-off above its peak rotation frequency, while free–free emission can continue with a relatively flat spectral slope.

To distinguish between these models, we compare the spectral models with the retrieved spectrum. We include a data point at 671 GHz ($F = 0.087^{+0.06}_{-0.05}$ mJy) from our posterior, in addition to the measurements by E. Macías et al. (2017) and A. A. Rota et al. (2024). We then search for models that reproduce this combined spectrum. For the free–free emission, we adopt the model described by P. G. Mezger & A. P. Henderson (1967), E. Keto (2003), and H. B. Liu et al. (2024):

$$F_{\rm ff} = B(\nu, T)(1 - e^{-\tau_{\rm ff}})\pi r_{\rm ff}^2, \qquad (21)$$

where $r_{\rm ff}$ is the radius of the free–free emission and the optical depth is given by

$$\tau_{\rm ff} = 8.235 \times 10^{-2}\left(\frac{T_{\rm ff}}{\rm K}\right)^{-1.35}\left(\frac{\nu}{\rm GHz}\right)^{-2.1}\left(\frac{\rm EM}{\rm pc\ cm^{-6}}\right), \qquad (22)$$

which includes the temperature $T_{\rm ff}$ and emission measure (EM). Due to the strong degeneracy between parameters, we fixed $r_{\rm ff} = 1.0$ au. For the spinning dust emission model, we employ the following equation from T. Hoang et al. (2018):

$$F_{\rm sd} = F_{\rm sd,0}\left(\frac{\nu}{\nu_{\rm pk}}\right)^2 \exp\left\{1 - \left(\frac{\nu}{\nu_{\rm pk}}\right)^2\right\}, \qquad (23)$$

where $F_{\rm sd,0}$ is the peak flux density and $\nu_{\rm pk}$ is the peak frequency.

We compared these models via χ^2 analysis against the retrieved spectrum, sampling the posterior distribution under broad priors using MCMC. In Figure 16, we plot the resulting best-fit (median) models. Under the free–free emission hypothesis, a combination of $T_{\rm ff} \sim 10^3$ K and EM $\sim 10^8$ pc cm^{-6} well reproduces the spectrum. Conversely, while the best-fit spinning dust model ($F_{\rm sd,0} \sim 0.1$ mJy and $\nu_{\rm pk} \sim 72$ GHz) is broadly consistent with the peak values reported by T. Hoang et al. (2018; $F_{\rm sd,0} \sim 0.6$ mJy and $\nu_{\rm pk} = 60$ GHz), it fails to reproduce the flat spectral slope at frequencies higher than the peak. In contrast, the free–free emission model remains consistent with the data across the entire range. Overall, we conclude that free–free emission is the more likely mechanism for the innermost region of the HD 169142 disk.

6. Summary

In this paper, we have presented `FRAP`, a new open-source framework designed to retrieve the physical properties of dust grains in protoplanetary disks directly from multiwavelength interferometric continuum observations. We validated the method using mock datasets and demonstrated its scientific capabilities by applying it to ALMA observations of the HD 169142 disk. The key features and results of `FRAP` are summarized as follows.

1. *Flexible physics-based modeling*. The radial profiles of dust properties, including surface density, temperature, and grain size distribution, are modeled as sample paths of GPs. This approach enables a highly flexible representation of disk structures while ensuring the intensity profiles are calculated through radiative transfer.
2. *Direct visibility fitting*. One-dimensional interferometric visibilities are derived from the intensity profiles via Hankel transforms. By comparing these models directly with observed visibilities across multiple frequencies, `FRAP` avoids the biases inherent in image-domain analysis. This also enables simultaneous model fitting to observations with different angular resolutions.
3. *Differentiable programming*. The framework is implemented using `JAX`, enabling end-to-end automatic differentiation. This significantly accelerates the sampling of posterior distributions, making robust Bayesian inference feasible for complex, multiparameter disk models.
4. *Superresolution and bias reduction*. Through injection–recovery tests, we demonstrated that `FRAP` provides significantly less biased estimates of dust properties than conventional radius-by-radius fitting. Notably, the method can resolve structures finer than the CLEAN beam, effectively achieving "superresolution."
5. *Application to HD 169142*. Applying `FRAP` to real ALMA data, we successfully retrieved the radial profiles of dust surface density, temperature, and grain size distribution index. Our results identified multiple rings and gaps, provided evidence for leaky dust traps, and distinguished between thermal-dust and free–free emission in the innermost disk. Additionally, we found that the temperature profile has a steep gradient at the inner edge of the inner ring. This is likely due to irradiation from the central star. The temperature at the inner side exceeds ∼100 K and the inner edge may correspond to the water snow line.

As ALMA and future facilities continue to provide high-resolution, multiband, and high-sensitivity datasets, such physics-based retrieval tools will become increasingly essential for deciphering the conditions of planet formation. `FRAP` is publicly available and being actively developed at https://github.com/tomyoshida/frap, with documentation at https://frap.readthedocs.io/. We welcome contributions from the community to further enhance the capabilities of this tool. The code version used for this paper is stored in a Zenodo repository at DOI: 10.5281/zenodo.20689546 (T. C. Yoshida et al. 2026).

Acknowledgments

We would like to thank the anonymous referee for helpful comments and suggestions. This paper makes use of the following ALMA data: ADS/JAO.ALMA#2018.1.01716.S, #2013.1.00592.S, #2015.1.00490.S, #2015.1.01301.S, #2016.1.00344.S, #2017.1.00727.S, and #2024.1.01254.S. ALMA is a partnership of ESO (representing its member states), NSF (USA), and NINS (Japan), together with NRC (Canada), NSTC and ASIAA (Taiwan), and KASI (Republic of Korea), in cooperation with the Republic of Chile. The Joint

ALMA Observatory is operated by ESO, AUI/NRAO, and NAOJ. T.C.Y. was supported by the ALMA Japan Research Grant of NAOJ ALMA Project, NAOJ-ALMA-385. This work was supported by Grant-in-Aid for JSPS Fellows, JP23KJ1008 (T.C.Y.). T.C.Y. and G.R. acknowledge support from the European Union (ERC Starting Grant DiscEvol, project No. 101039651) and from Fondazione Cariplo, grant No. 2022-1217. S.F. acknowledges financial contribution from the European Union (ERC, UNVEIL, 101076613). Views and opinions expressed are, however, those of the author(s) only and do not necessarily reflect those of the European Union or the European Research Council. Neither the European Union nor the granting authority can be held responsible for them.

Facility: ALMA.

Software: `JAX` (J. Bradbury et al. 2018), `numpyro` (E. Bingham et al. 2019; D. Phan et al. 2019), astropy (Astropy Collaboration et al. 2013, 2018, 2022), CASA (CASA Team et al. 2022).

Appendix A
Visibilities of Axisymmetric Source with Primary Beam Correction

In previous studies such as `frankenstein` (J. Jennings et al. 2020), the antenna primary beam was not taken into account during modeling, leaving the retrieved intensity profiles affected by primary beam attenuation. This has not been a significant issue because the primary beam is sufficiently larger than the typical disk radius in most cases. Additionally, since these studies focused on the intensity profile at a single frequency, which is proportional to the primary beam, the resultant profiles could simply be understood as the product of the actual profile and the primary beam.

However, in `FRAP`, we should explicitly take this effect into account because the retrieved quantities are now physical parameters, which are no longer proportional to the primary beam. The measurement equation of interferometry with the primary beam correction is

$$\mathcal{V}(u, v) = \int_{-\infty}^{\infty} dl \int_{-\infty}^{\infty} dm\, A(l, m) I(l, m) e^{-2\pi i(ul+vm)}, \quad \text{(A1)}$$

where $\mathcal{V}(u, v)$ is the visibility at spatial frequencies (u, v), $A(l, m)$ is the primary beam at sky coordinates (l, m), and I is the intensity distribution on the plane of the sky. In our problem setting, we consider a geometrically thin, axisynmetric disk with a PA $\theta_{\rm PA}$ and inclination angle $\theta_{\rm incl}$. We also assume that the disk center is located at the phase center. Here, we define spatial coordinates on the disk plane (l', m') and coresponding coordinates in the Fourier domain (u', v'). Those coordinates are related to the original ones with

$$\begin{pmatrix} l' \\ m' \end{pmatrix} = \begin{pmatrix} 1/\cos\theta_{\rm incl} & 0 \\ 0 & 1 \end{pmatrix} \begin{pmatrix} \cos\theta_{\rm PA} & -\sin\theta_{\rm PA} \\ \sin\theta_{\rm PA} & \cos\theta_{\rm PA} \end{pmatrix} \begin{pmatrix} l \\ m \end{pmatrix}, \quad \text{(A2)}$$

and

$$\begin{pmatrix} u' \\ v' \end{pmatrix} = \begin{pmatrix} \cos\theta_{\rm incl} & 0 \\ 0 & 1 \end{pmatrix} \begin{pmatrix} \cos\theta_{\rm PA} & -\sin\theta_{\rm PA} \\ \sin\theta_{\rm PA} & \cos\theta_{\rm PA} \end{pmatrix} \begin{pmatrix} u \\ v \end{pmatrix}. \quad \text{(A3)}$$

The deprojected equation can be expressed as

$$\mathcal{V}'(u', v') = \cos\theta_{\rm incl} \int_{-\infty}^{\infty} dl' \int_{-\infty}^{\infty} \times dm' A'(l', m') I'(l', m') e^{-2\pi i(u'l'+v'm')}, \quad \text{(A4)}$$

where A' and I' are the primary beam and intensity distribution in the deprojected coordinates, respectively. We assume that those values are the same as those in the original coordinates (e.g., M. Aizawa et al. 2024):

$$A'(l', m') = A(l, m), \quad \text{(A5)}$$

$$I'(l', m') = I(l, m). \quad \text{(A6)}$$

We can convert Equation (A4) to polar coordinates:

$$\mathcal{V}''(q, \varphi) = |\cos\theta_{\rm incl}| \int_{-\pi}^{\pi} d\phi \int_{0}^{\infty} \times r dr A''(r, \phi) I''(r) e^{-2\pi i qr\cos(\phi-\varphi)}, \quad \text{(A7)}$$

where $q = \sqrt{u'^2 + v'^2}$, $\varphi = \arctan(v'/u')$, $r = \sqrt{l'^2 + m'^2}$, and $\phi = \arctan(l'/m')$. A'' and I'' are, respectively, the primary beam and intensity distribution in polar coordinates. Since we consider axisymmetric disk, I'' depends only on r. However, the "deprojected" primary beam, which was initially circular, is now instead elliptical and has a dependency on ϕ.

Here, we introduce Fourier series expansion of A'' in the ϕ direction:

$$A''(r, \phi) = \sum_{m=-\infty}^{\infty} A''_m(r) e^{im\phi}, \quad \text{(A8)}$$

where m indicates a mode, and $A''_m(r)$ is the Fourier coefficient

$$A''_m(r) = \frac{1}{2\pi} \int_0^{2\pi} d\phi\, A''(r, \phi) e^{-im\phi}. \quad \text{(A9)}$$

By substituting Equation (A7) into Equation (A8), we obtain

$$\mathcal{V}''(q, \varphi) = |\cos\theta_{\rm incl}| \int_0^{\infty} dr\, I''(r) r \times \sum_{m=-\infty}^{\infty} A''_m(r) \int_{-\pi}^{\pi} d\phi\, e^{i\{m\phi - 2\pi qr\cos(\phi-\varphi)\}}. \quad \text{(A10)}$$

Using the mth-order Bessel function of the first kind, J_m, the ϕ integral can be further reduced to be

$$\int_{-\pi}^{\pi} d\phi\, e^{i\{m\phi - 2\pi qr\cos(\phi-\varphi)\}} = 2\pi(-i)^m e^{im\varphi} J_m(2\pi qr), \quad \text{(A11)}$$

therefore:

$$\mathcal{V}''(q, \varphi) = 2\pi |\cos\theta_{\rm incl}| \int_0^{\infty} dr\, I''(r) r \times \sum_{m=-\infty}^{\infty} A''_m(r) (-i)^m e^{im\varphi} J_m(2\pi qr). \quad \text{(A12)}$$

In FRAP, we aim to fit the azimuthally averaged deprojected visibility profiles. Therefore, the quantity we compare is

$$\begin{aligned}\mathcal{V}_{\rm mod} &= \langle \mathcal{V}''(q, \varphi)\rangle_\phi \\ &= \frac{1}{2\pi}\int_{-\pi}^{\pi} d\varphi\ 2\pi|\cos\theta_{\rm incl}|\int_0^\infty dr\ I''(r)r \\ &\quad\times\sum_{m=-\infty}^{\infty} A''_m(r)(-i)^m e^{im\varphi}J_m(2\pi qr) \\ &= |\cos\theta_{\rm incl}|\int_0^\infty dr\ I''(r)rA''_0(r)J_0(2\pi qr), \end{aligned} \tag{A13}$$

because $e^{im\varphi}$ vanishes for $m \neq 0$ after integration by φ. Here, $A''_0(r)$ is the averaged primary beam at each disk radius and can be calculated by Equation (A9).

These results are consistent with the conventional Hankel transform expression of visibilities (e.g., R. N. Bracewell 2000; J. Jennings et al. 2020; M. Aizawa et al. 2024), except for the primary beam correction. The equation becomes identical to the previous one if we take $A''_0(r) = 1$. By replacing the intensity profile in Equation (3) of J. Jennings et al. (2020) by $A''_0(r)I''(r)$, we obtain Equation (8). Note that we use $A_{\rm eff}(\nu, r)$ instead of $A''_0(r)$ in the main text for a consistent notation.

Appendix B
Intensities and Optical Depths of the Mock Data

Figure 18 presents the radial profiles of the intensities and optical depths for each band in the mock datasets analyzed in Section 3. The inner ring is marginally optically thick even in Band 3. In contrast, the outer rings remain optically thin, particularly in Bands 3, but become moderately optically thick in other bands.

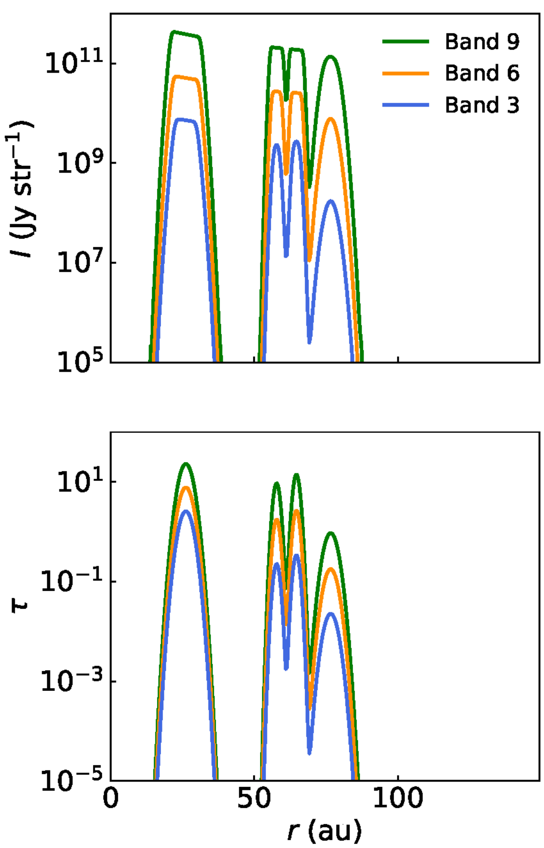

Figure 18. Input radial profiles of the intensities and optical depths for the mock data.

Appendix C
Estimated Dust Mass in the Injection–Recovery Test

Figure 19 presents the posterior distribution of the dust mass at $r > 46$ au for various l_X in the injection–recovery tests (Section 3.3.2). We also plot the results from the image-based conventional method (Section 3.2) for comparison. The estimated masses are reasonably consistent with the input value if $l_X < 0\farcs03$, while larger l_X values and conventional methods significantly overestimate it. Note that the $l_X = 0\farcs03$ (SB + LB) case has a prominent peak of the distribution at a higher mass than the truth, however, this is primarily due to the marginalization effect of the Bayesian analysis and the true value is still covered within the distribution.

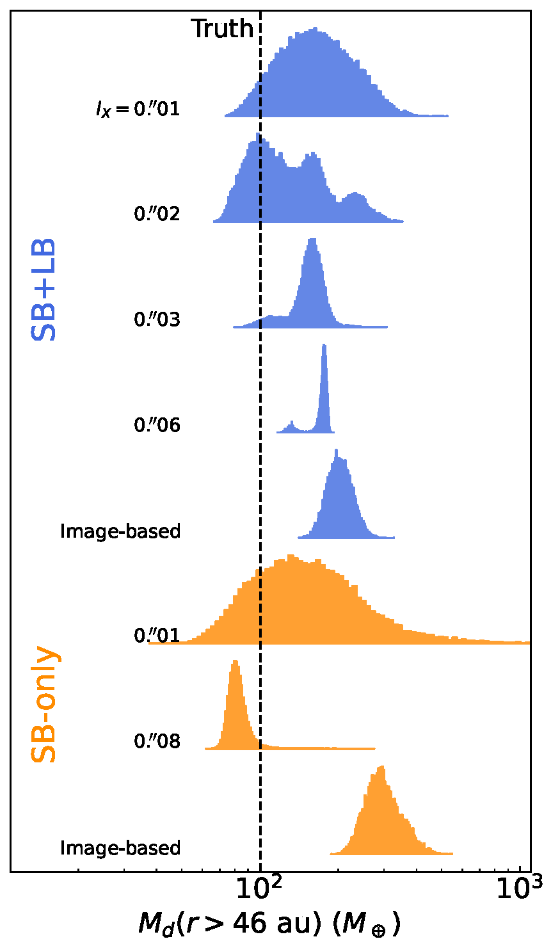

Figure 19. Posterior distributions of the dust mass at $r > 46$ au for various l_X values and image-based conventional methods. The black vertical line indicates the input truth.

Appendix D
Injection–Recovery Test with q as a Free Parameter

In Section 3.3.2, we demonstrate FRAP with the power-law index of the grain size distribution, q, being a fixed parameter for simpler interpretation of the results. We also perform the same posterior sampling but make q free. Here, the prior range of q is set to be [1, 5]. The other configurations are the same as the $l_X = 0\farcs03$ case in Section 3.3.2. Figure 20 shows the posterior distribution. The uncertainties become larger than the fixed-q case in Figure 6, however, the posteriors are still consistent with the input profiles.

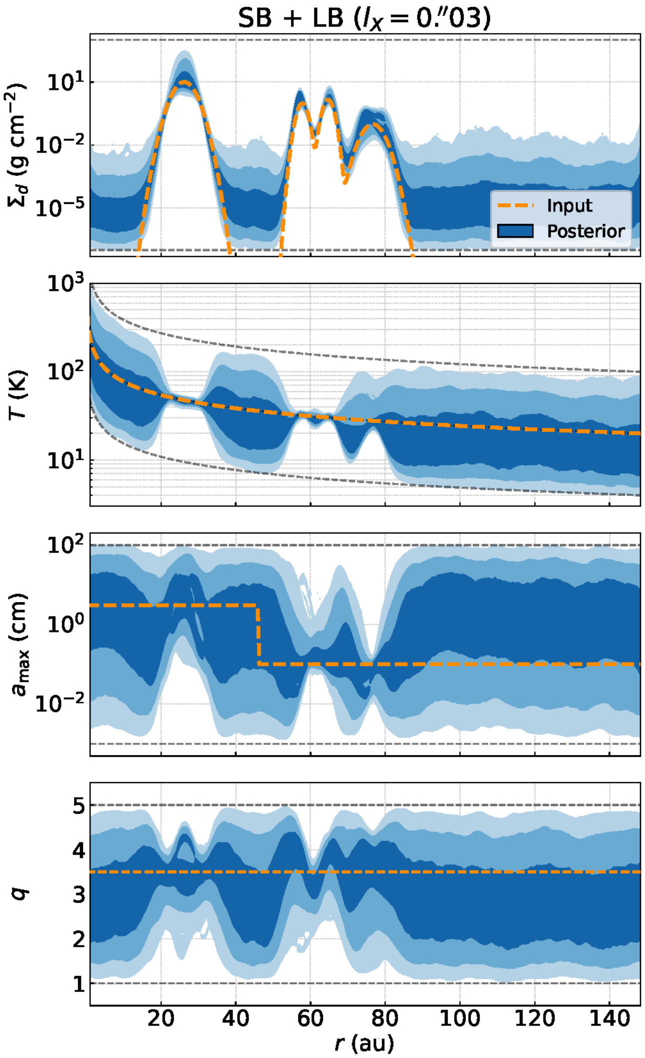

Figure 20. Same as the left panel of Figure 6, but with q added as a free parameter.

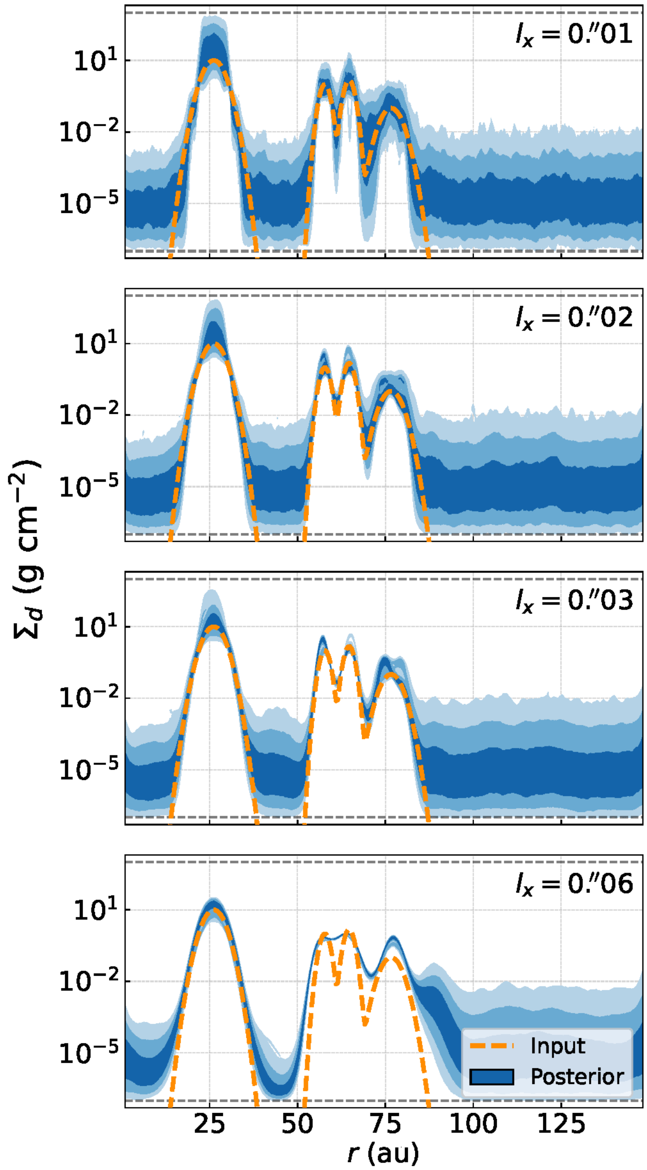

Figure 21. Comparison of the posterior distribution of Σ_d for various l_X.

Appendix E
Sensitivity on the Length Scale Parameter

In Section 3.3.4, we mentioned that a smaller length scale parameter allows higher flexibility, resulting in less biased but larger uncertainty. To show this behavior more clearly, we additionally ran posterior sampling with $l_X = 0.''02$, $0.''06$, and $0.''08$. In Figure 21, a comparison of the resultant dust surface density profiles, including the cases with $l_X = 0.''01$ and $0.''03$, is presented. This shows the sensitivity of the results on the length scale parameter. As long as the prior can express the physical profiles (i.e., sufficiently small l_X), the results are not biased.

Appendix F
Observational Details

Table 2 summarizes the details of the observations for the HD 169142 disk.

Table 2
Summary of ALMA Observations

Project Code	PI	Date	On-source Time (minutes)	Baselines (m)	Frequencies[a] (GHz)
			Band 3		
2018.1.01716.S	E. Macías	2019 Jun 21	41.5	80–14,373	90.5, 92.4, 102.5, 104.5
…	…	2019 Jun 25	41.4	82–16,196	90.5, 92.4, 102.5, 104.5
…	…	2019 Jun 25	41.6	250–16,185	90.5, 92.4, 102.5, 104.5
…	…	2019 Jun 25	41.4	81–15,306	90.5, 92.4, 102.5, 104.5
…	…	2019 Sep 1	21.3	31–3562	90.5, 92.4, 102.5, 104.5
…	…	2019 Sep 3	21.3	38–3617	90.5, 92.4, 102.5, 104.5
			Band 6		
2013.1.00592.S	D. Fedele	2015 Aug 30	4.7	13–1447	216.1, 219.5, 220.4, 230.5, 233.0
2015.1.00490.S	M. Honda	2016 Sep 14	3.6	14–3195	219.5, 220.4, 230.5, 233.0
…	…	2016 Sep 14	3.6	13–2962	219.5, 220.4, 230.5, 233.0
…	…	2016 Sep 14	3.6	15–2648	219.5, 220.4, 230.5, 233.0
2015.1.01301.S	J. Hashimoto	2016 Sep 17	3.1	14–2293	219.5, 220.4, 230.5, 232.5
2016.1.00344.S	S. Pérez	2016 Oct 4	4.5	18–2675	218.0, 219.5, 220.4, 230.5, 232.0
…	…	2017 Jul 5	4.5	17–2626	218.0, 219.6, 220.4, 230.5, 232.0
…	…	2017 Sep 18	19.1	41–11,877	218.0, 219.5, 220.4, 230.5, 232.0
…	…	2017 Sep 19	19.1	41–11,471	218.0, 219.5, 220.4, 230.5, 232.0
…	…	2017 Nov 9	19.2	101–13,207	218.0, 219.5, 220.4, 230.5, 232.0
			Band 9		
2017.1.00727.S	J. Szulágyi	2019 Aug 14	15.4	41–3111	660.9, 661.0, 664.0, 664.2, 677.0 677.2, 680.1, 680.2
…	…	2019 Aug 14	13.4	39–3013	660.9, 661.0, 664.0, 664.2, 677.0 677.2, 680.1, 680.2
2024.1.01254.S	T. Yoshida	2024 Oct 11	6.5	14–475	660.0, 662.0, 664.0, 666.0, 676.0 678.0, 680.0, 682.0

Notes. This table is generated by `tabgenalma` (https://github.com/tomyoshida/tabgenalma).
[a] Mean frequency of spectral windows.

ORCID iDs

Tomohiro C. Yoshida https://orcid.org/0000-0001-8002-8473
Enrique Macías https://orcid.org/0000-0003-1283-6262
Giovanni Rosotti https://orcid.org/0000-0003-4853-5736
Stefano Facchini https://orcid.org/0000-0003-4689-2684
Elena Viscardi https://orcid.org/0009-0005-5187-6074
Kiyoaki Doi https://orcid.org/0000-0003-1958-6673

References

Aizawa, M., Muto, T., & Momose, M. 2024, MNRAS, 532, 1361
Andrews, S. M., Huang, J., Pérez, L. M., et al. 2018, ApJL, 869, L41
Astropy Collaboration, Price-Whelan, A. M., Lim, P. L., et al. 2022, ApJ, 935, 167
Astropy Collaboration, Price-Whelan, A. M., Sipőcz, B. M., et al. 2018, AJ, 156, 123
Astropy Collaboration, Robitaille, T. P., Tollerud, E. J., et al. 2013, A&A, 558, A33
Baddour, N., & Chouinard, U. 2015, JOSAA, 32, 611
Benisty, M., Bae, J., Facchini, S., et al. 2021, ApJL, 916, L2
Bingham, E., Chen, J. P., Jankowiak, M., et al. 2019, JMLR, 20, 28
Birnstiel, T., Dullemond, C. P., Zhu, Z., et al. 2018, ApJL, 869, L45
Birnstiel, T., Ormel, C. W., & Dullemond, C. P. 2011, A&A, 525, A11
Booth, A. S., Law, C. J., Temmink, M., Leemker, M., & Macías, E. 2023, A&A, 678, A146
Bracewell, R. N. 2000, The Fourier Transform and its Applications (McGraw Hill)
Bradbury, J., Frostig, R., Hawkins, P., et al. 2018, JAX: composable transformations of Python+NumPy programs, 0.3.13, http://github.com/jax-ml/jax
Bruderer, S. 2013, A&A, 559, A46
Carrasco-González, C., Sierra, A., Flock, M., et al. 2019, ApJ, 883, 71
Carvalho, A. S., Pérez, L. M., Sierra, A., et al. 2024, ApJ, 971, 129
CASA Team, Bean, B., Bhatnagar, S., et al. 2022, PASP, 134, 114501
Cortes, P., Carpenter, J., Kameno, S., et al. 2025, ALMA Cycle 12 Technical Handbook, Zenodo, doi:10.5281/zenodo.14933753
Dickinson, C., Ali-Haïmoud, Y., Barr, A., et al. 2018, NewAR, 80, 1
Dohnanyi, J. S. 1969, JGR, 74, 2531
Doi, K., & Kataoka, A. 2023, ApJ, 957, 11
Doi, K., Kataoka, A., Liu, H. B., et al. 2024, ApJL, 974, L25
Fedele, D., Carney, M., Hogerheijde, M. R., et al. 2017, A&A, 600, A72
Francis, L., Johnstone, D., Herczeg, G., Hunter, T. R., & Harsono, D. 2020, AJ, 160, 270
Fukagawa, M., Tamura, M., Itoh, Y., et al. 2010, PASJ, 62, 347
Gaia Collaboration, Vallenari, A., Brown, A. G. A., et al. 2023, A&A, 674, A1
Garg, H., Pinte, C., Hammond, I., et al. 2022, MNRAS, 517, 5942
Guerra-Alvarado, O. M., Carrasco-González, C., Macías, E., et al. 2024, A&A, 686, A298
Guidi, G., Isella, A., Testi, L., et al. 2022, A&A, 664, A137
Hammond, I., Christiaens, V., Price, D. J., et al. 2023, MNRAS, 522, L51
Hoang, T., Lan, N.-Q., Vinh, N.-A., & Kim, Y.-J. 2018, ApJ, 862, 116
Hoffman, M. D., & Gelman, A. 2014, JMLR, 15, 1593
Honda, M., Maaskant, K., Okamoto, Y. K., et al. 2012, ApJ, 752, 143
Ilee, J. D., Walsh, C., Jennings, J., et al. 2022, MNRAS, 515, L23
Jennings, J., Booth, R. A., Tazzari, M., Rosotti, G. P., & Clarke, C. J. 2020, MNRAS, 495, 3209
Keto, E. 2003, ApJ, 599, 1196
Leemker, M., Booth, A. S., van Dishoeck, E. F., et al. 2022, A&A, 663, A23
Li, D., Liu, Y., Wang, H., Fang, M., & Wang, L. 2024, A&A, 688, A204
Liu, H. B. 2019, ApJL, 877, L22
Liu, H. B., Casassus, S., Dong, R., et al. 2024, ApJ, 972, 163
Loomis, R. A., Facchini, S., Benisty, M., et al. 2025, ApJL, 984, L7
Lucas, M., Bottom, M., Dong, R., et al. 2025, AJ, 170, 278
Macías, E., Anglada, G., Osorio, M., et al. 2017, ApJ, 838, 97
Macías, E., Guerra-Alvarado, O., Carrasco-González, C., et al. 2021, A&A, 648, A33
Macías, E., Espaillat, C. C., Osorio, M., et al. 2019, ApJ, 881, 159
Mathis, J. S., Rumpl, W., & Nordsieck, K. H. 1977, ApJ, 217, 425
Mezger, P. G., & Henderson, A. P. 1967, ApJ, 147, 471
Miyake, K., & Nakagawa, Y. 1993, Icar, 106, 20
Momose, M., Morita, A., Fukagawa, M., et al. 2015, PASJ, 67, 83
Ohashi, S., Momose, M., Kataoka, A., et al. 2023, ApJ, 954, 110
Osorio, M., Anglada, G., Carrasco-González, C., et al. 2014, ApJL, 791, L36
Pérez, S., Casassus, S., Baruteau, C., et al. 2019, AJ, 158, 15
Phan, D., Pradhan, N., & Jankowiak, M. 2019, arXiv, arXiv:1912.11554
Pinilla, P., Benisty, M., Waters, R., Bae, J., & Facchini, S. 2024, A&A, 686, A135
Quanz, S. P., Avenhaus, H., Buenzli, E., et al. 2013, ApJL, 766, L2
Rampinelli, L., Facchini, S., Leemker, M., et al. 2026, ApJL, 996, L17

Ricci, L., Testi, L., Natta, A., et al. 2010, A&A, 512, A15
Rosotti, G. P., Tazzari, M., Booth, R. A., et al. 2019, MNRAS, 486, 4829
Rota, A. A., Meijerhof, J. D., van der Marel, N., et al. 2024, A&A, 684, A134
Sierra, A., & Lizano, S. 2020, ApJ, 892, 136
Sierra, A., Pérez, L. M., Sotomayor, B., et al. 2024, ApJ, 974, 306
Sierra, A., Pérez, L. M., Zhang, K., et al. 2021, ApJS, 257, 14
Sierra, A., Pinilla, P., Pérez, L. M., et al. 2025, MNRAS, 538, 2358
Tanaka, H., Inaba, S., & Nakazawa, K. 1996, Icar, 123, 450
Teague, R. 2019, JOSS, 4, 1632
Thompson, A. R., Moran, J. M., & Swenson, G. W., Jr. 2017, Interferometry and Synthesis in Radio Astronomy (3rd ed.; Springer)
Ueda, T., Kataoka, A., & Tsukagoshi, T. 2022, ApJ, 930, 56
Virtanen, P., Gommers, R., Oliphant, T. E., et al. 2020, NatMe, 17, 261
Viscardi, E. M., Macías, E., Zagaria, F., et al. 2025, A&A, 695, A147
Yoshida, T. C., Macías, E., Rosotti, G., et al. 2026, Flexible Radial Analysis of Protoplanetary disks: FRAP v1.0.0, Zenodo, doi:10.5281/zenodo.20689546
Yoshida, T. C., Nomura, H., Tsukagoshi, T., et al. 2025, ApJ, 980, 50
Zagaria, F., Facchini, S., Curone, P., et al. 2025, A&A, 702, A56
Zhang, S., Zhu, Z., Ueda, T., et al. 2023, ApJ, 953, 96
Zhu, Z., Zhang, S., Jiang, Y.-F., et al. 2019, ApJL, 877, L18